Assessment of Image Quality of a PET/CT scanner for a Standarized Image situation Using a NEMA Body Phantom

"The impact of Different Image Reconstruction Parameters on Image quality"

by

QUAYE MICHAEL

This thesis is submitted in partial fulfilment of the requirements for the degree of Master in Medical Biology – Biomedical Image Sciences

Department of Biomedicine / Haukeland University Hospital (Nuclear Medicine Department)

Supervisor:	Dr Odd Harald Odland
Co- supervisor:	Kristine Eldevik Fasmer
Co- supervisor:	Prof. Arvid Lundervold

University of Bergen

August 2013

ACKNOWLEDGEMENT

I would first of all thank the ALMIGHTY JEHOVAH for the strength, guidance and knowledge throughout my studies.

I would also like to thank all the people who have helped, contributed and encouraged me during my thesis work.

To my supervisor Dr Odd Harald Odland, thank you for introducing me to the project and making it known to me the Physics involved in this thesis work. You have helped and supported me during this project. You have been my advisor even when sometimes communication was a problem. It would have been difficult to do this work on my own.

My co-supervisor Kristine Eldevik Fasmer has been more than my help, motivation and idea behind my work. She has given me most of the background understanding of the terms in my work. Thank you for being strict and at same time fair on correcting my work and above all for spending time on my thesis work.

Prof. Arvid Lundervold has been my motivation from the start of the work. Upon all his busy schedules, he still finds time for me whenever I call to meet him. Thank you for the encouragement you have always given me.

Jostein Sæterstøl, thank you for spending those precious times of your work schedules to help me whenever I call on you. Also to Njål Brekke, for developing the automatic python program used in this work and for the enlightening discussions.

To the wonderful people at the PET centre at Haukeland University Hospital that has spent time explaining the PET/CT system to me, showing interest and making the scanner available for experiment, thank you.

My family for being there for me, encouraging and ensuring my well being. I love you all.

Bergen, August 30th 2013

Michael Quaye

Table of contents

Summary and Aim of this work

Radiologists and medical practitioners are working daily with images from integrated Positron Emission Tomography/ Computed Tomography (PET/CT) scanners in order to detect potentially lethal diseases. It is thus very important to ensure that these images have adequate image quality. For the staff responsible of quality assurance of the applied scanner, it is important to ensure that the reconstruction procedures and image protocols in use enable acquisition of image with a high quality with respect to resolution and contrast, while the data sets are containing as little noise as possible. The goal of the quality assurance work will be to continuously make sure that, data acquisition settings and especially the reconstruction procedure that is utilized for routine and daily clinical purposes, enables lesions or cancer cells and diseases to be detected.

This master thesis project aims at evaluating a reconstruction algorithm (iterative reconstruction) and some key parameters applied in image reconstruction. These parameters include selected filters (Gaussian, median, Hann and Butterworth filter), selected full width at half maximum values (FWHM: 3, 5, and 7 mm) and image matrix sizes (128 x 128 and 168 x 168 pixels respectively), in order to provide information on how these key parameters will affect image quality.

The National Electrical Manufacturers Association (NEMA) International Electrotechnical Commission (IEC) Body Phantom Set was used in this work. It consists of a lid with six fillable spheres (with internal diameters 37, 28, 22, 17, 13 and 10 mm respectively), lung insert, body phantom (which represent the background volume) and a test phantom.

The work in this thesis project has been carried out using the radiopharmaceutical tracer an F-18 FDG, fluotodeoxyglucose, produced with a cyclotron, a General Electric's PETtrace 6 cyclotron, at the Center for Nuclear Medicine/PET at Haukeland University Hospital in Bergen, Norway.

The applied radiopharmaceutical F-18 FDG was produced in a 2.5 ml target volume at the cyclotron. After the production, this volume was delivered from the cyclotron into a 20 ml sealed cylindrical glass already containing 17.5 ml of non-radioactive water. The activity

level in this new solution with 20 ml F-18 FDG and water was measured in a dose calibrator (ISOMED 2010^{TM}). The solution was diluted further, in an iterative process, a number of times in order to acquire the necessary activity concentrations for both the selected hot spheres and the background volume. The aim was to obtain activity concentrations for sphere-to-background ratios of either 4:1 or 8:1. The sphere-to-background ratio in this work is the ratio between the radioactivity level in four small spheres (with diameters 22, 17, 13 and 10 mm respectively, and having a total volume of 9.8 ml for all the 4 spheres) and the radioactivity level in the main body of the applied phantom; the so-called background volume (9708 ml). The two bigger spheres (28 and 37 mm) were filled with non-radioactive water in order to represent areas without radioactivity, i.e. "cold spheres".

When the spheres and volumes under study were filled with the desired level of activity and the activity level was measured, the spheres were positioned into the applied body phantom and the phantom was sealed to avoid spillage.

The prepared NEMA IEC body phantom was placed on the table of a Siemens Biograph 40 PET/CT scanner in a predetermined reproducible position and scanned using a standard clinical whole body PET/CT protocol. The acquired images were reconstructed. Three repetitive studies were done for each concentration ratio. For each experiment performed, the sphere-to-background ratios were either 4:1 or 8:1. A selection of different standardized reconstruction parameters and different image corrections were applied. This was done in order to study what impact changes of the reconstruction parameters will have on the image quality. The image quality being defined by a quantification of the measured relative contrast in the images studied. The procedures followed while performing the PET/CT were in compliance with the recommended procedure presented in the NEMA NU2 – 2007 manual (from the manufacturer of the NEMA IEC body phantom described above).

The reconstructed images were analyzed manually on a PET/CT workstation and also analyzed automatically with python programming software specially developed for the purpose of this work. The image quality results obtained from analyzes of the reconstructed images when different reconstruction parameters were used, were thereafter compared to the standardized protocol for reconstruction of PET/CT images. Lastly, the results have been compared with other similar work on the same subject by Helmar Bergmann et al (2005).

List of Abbreviations

Abbreviation	Description
ACD	Annihilation Coincidence Detection
CAT	Computed Axial Tomography
CT	Computed Tomography
DICOM	Digital Image and Communications in Medicine
FBP	Filtered Back Projection
FDG	Fluorodeoxyglucose
FWHM	Full Width at Half Maximum
IEC	International Electrotechnical Commission
LOR	Line Of Response
MS	Matrix Size
NEMA	National Electrical Manufacturers Association
OSEM	Ordered Subset Expectation Maximization
PET	Positron Emission Tomography
PMT	Photo Multiplier Tube
PVE	Partial Volume Effect
ROI	Region of Interest
SPECT	Single Photon Emission Computed Tomography
SPSS	Statistical Product and Service Solution

List of Figures

1. Introduction

Nuclear medicine represents an aspect of medicine where radioactive pharmaceuticals are administered to a patient, and the distribution of these radiopharmaceuticals in the patient's body can be observed in dedicated detectors, which often are referred to as scanners. The distribution of the radiopharmaceutical in the body (the "uptake") will bring information about a patient's health to a trained doctor.

The type of clinical information that is obtained from the study of the distribution of the pharmaceuticals administered into a patient will depend on which type of radiopharmaceutical that is administered [17].

The quantification of the information from Positron Emission Tomography PET and integrated Positron Emission Tomography/ Computed Tomography (PET/CT) images is the basis for an essential technique in staging cancer disease, monitoring the development of cancer disease and in assessment of treatment responses. In order to evaluate the quality of the data or image to be staged, assessed and monitored, certain criteria need to be defined. In addition, some quantitative (objective) measures are applied to these criteria, with which the quality of the acquired data (the image) can be measured.

1.1 Nuclear Medicine

The pharmaceuticals or radioactive elements (described in Chapter 1.4.2) administered to the patients were termed *radio-tracers* by George de Hevesy in the 1920s. One significant characteristic of a tracer is the ability to assist in the study of the components (of the human body) making up a homeostatic system without causing changes in their function. Before this knowledge was established, Irene Curie and Frederic Joliot, in the 1930s, discovered the artificial radioactivity. Following that, Ernest Lawrence developed the cyclotron; and these two discoveries made it possible for the radiotracers to be produced from many elements. This enabled development of particular biochemical processes as the basis for the evolution of radiopharmaceuticals (radiotracers) for diagnosing and staging of cancer disease [1].

Since the invention of the *gamma camera,* which was first introduced in 1985 by Hal Anger, nuclear medicine has changed dramatically due to the way diseases could be visualized. This is achieved by rendering images of the distributions of radiotracers and biochemical functions of the body [1].

1.2 Radioactivity and ionising radiation

Radioactivity is the spontaneous disintegration (by emission of radiation) of atomic nuclei [18d][27][28]. The emission of radiation by radio nuclides are normally arranged into classes. Thus radiation is mainly divided into electromagnetic radiation: which pertains to magnetism produced by electric charges in motion such as x-rays, γ (gamma) rays, annihilation photons and particle radiation: which consist of distinct particles such as β^- (beta minus), β^+ (beta plus), or (alpha) particles [1]. Radiation implies a transition of energy (energetic particles) from an object, which is the source, through space to another object, the target, where it is potentially absorbed. Radiation is a spontaneous transformation process whereby one or more stable daughter nuclei are formed from unstable parent nuclei [18d] [27] [28].

A general radioactive decay process can be quantified and represented in a simple mathematical equation form as

$$N = N_0 e^{-\lambda t} \qquad \{1.1\}$$

Where N_0 is the number of radioactive nuclei at time t = 0, N is the number of radioactive nuclei at time t, and λ is the decay constant of the radionuclide. The decay constant, λ is the disintegration of a fraction of an atom per unit time [20].

The activity, *A*, is rate at which the radioactive nuclei undergoes a transition. It can be denoted as follows:

$$A = \left|\frac{dN(t)}{dt}\right| = \lambda N = \lambda N_0 e^{-\lambda t} = A_0 e^{-\lambda t} \qquad \{1.2\}$$

Where $A_0 = \lambda N_0$ is the initial activity of the radioactive nuclei [27][28].

The half-life of a radioactive nuclei (a radioisotope), $t_{1/2}$ is the required time for one-half of the radioactive nuclei, measured at a certain time (t = 0) to disintegrate. The half-life of

radioactive nuclei is related to the decay constant, and the relation between the half-life and the decay constant can be expressed as shown in equation {1.3} [28]:

$$N = \frac{N_o}{2} = N_o e^{-\lambda t_{1/2}} \Rightarrow t_{1/2} = \frac{\ln 2}{\lambda} \qquad \{1.3\}$$

1.2.1 Radioactive decay modes

A decay process results in the emission of a certain type of radiation depending on the mode of decay. The three main radiation decay modes are $\alpha-$, $\beta-$ and $\gamma-$ decay.

The PET principle is based on detection of positron emission from radioactive nuclei. This is a technique that makes use of radiation decay mode of β^+ emitters. These are nuclides (isotopes) rich in proton(s). In positron decay, a proton is transformed into a neutron, a positron, and an electron neutrino in a spontaneous disintegration into a more stable energy state than the original isotope exhibited. This process is shown in equation {1.4}:

$$p \rightarrow n + e^+ + v \qquad \{1.4\}$$

Where: $p-$ proton, $n-$ neutron, e^+- positron and $v-$ electron neutrino. The positron (β^+) energy is distributed continuously in its spectrum. The energies of the distributed positrons range from 0 to $E_\beta^{\max}$ (the maximum energy), shown in figure 1.1 below. The electron neutrino carries away with it the energy difference between the energy of the original proton and the energy of the positron and the neutron. One possible outcome of positron emission is described in Chapter 2.6, positron annihilation and emission of two, oppositely $\gamma-$ quanta directed away from the annihilation point [1][28].

On the other hand, nuclides rich in neutron(s) are transformed into proton, an electron and an antineutrino. Thus, a radiation decay mode with electron emission.

$$n \rightarrow p + e^- + \bar{v} \qquad \{1.5\}$$

Where: $n-$ neutron, $p-$ proton, e^- – electron and $\bar{v}-$ antineutrino. The excess energy of the transformation process is shared between the proton, the electron and the electron antineutrino [28].

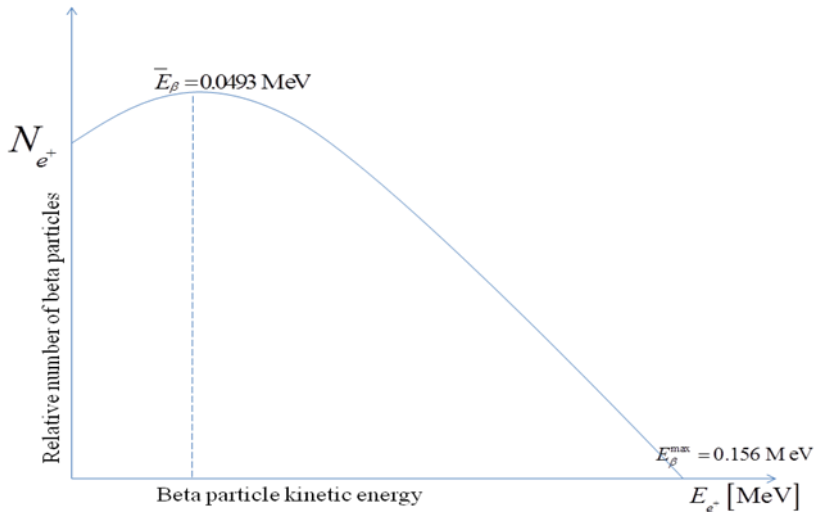

Figure 1.1: The energy distribution of positrons in a $\beta^+ -$decay of the isotope ^{14}C. The maximum energy is represented by $E_\beta^{\max}$ (0.156 MeV) and the average energy is represented $\overline{E}_\beta$ (0.0493 MeV). *[Adapted from* [29]*]*

In the process of radioactive decays, the daughter nucleus produced after radioactive decay remains in an excited state if it has not reached the ground state. In the process of entering into the ground state, gamma photons are emitted in a process known as $\gamma -$decay mode. The extra energy from the process is carried away by the gamma photon as kinetic energy. The detection of gamma photons is central in this work [28].

Interaction between photons and matter

When gamma rays (photons) traverses into a sample of matter, the interaction between the photons and the matter traversed will induce a series of fundamental processes. By this interaction the incoming radiation interacts with the nucleus and electrons of the atoms in the matter traversed.

There are four main processes that may occur during an interaction between photons and matter. These processes are;

1) The photoelectric effect
2) The Compton Effect (scattering)
3) The Rayleigh-Thompson effect

4) And for higher energies than 1.022 MeV (twice the electron rest mass), pair production take place.

1.3 The Photoelectric effect

When a photon passes through an absorber, the photon interacts with an electron in the inner shell. The photon in this interaction ceases to exist (it is absorbed) as its total energy is transferred to the electron. In this process the interacting electron is ejected from its orbit, e.g. normally the K-shell creating a vacancy in the orbit. The ejected electron has a kinetic energy, $E_{electron}$, that is equal to the difference between the energy of the incoming gamma photon, E_γ and the binding energy of the ejected electron, E_B (that is: $E_{electron} = E_\gamma - E_B$). The probability for the photoelectric effect to occur is proportional to the absorber's atomic number (thus, it increases with increasing atomic number of the absorber) but decreases as the gamma photon's energy increases. The relation between atomic number Z and the gamma photon's energy E_γ is given by Z^5 / E_γ^3. As the electron is ejected, the vacancy created is filled in by an electron transition from a higher shell (e.g. L-shell). The transition process involves the emission of energy by the emission of an x-ray photon; this is known as the characteristic x-ray. The emitted photon carries with it the energy difference between the two shells involved (very often the K and L-shell) [22b] [28].

1.4 The Compton scattering

In Nuclear Medicine, the energy range for gamma radiation is normally between 80 to 511 keV (see figure 1.3), the latter being the energy related to positron emission. The Compton Effect is the predominant process, or effect, in the above range of energy; being also the region for biological tissues (which are mainly made up of water). In the Compton Effect a photon interacts with the orbit electron of an atom and deposits part of its energy to the orbit electron ejecting it in the process. This interaction causes the photon to be deflected (figure 1.2) at an angle, θ_p and the ejected orbit electron recoils [25]. The ejected orbital electron is referred to as the Compton electron. It carries energy, E_e made up of the difference between part of the $\gamma-$ray's energy, $E_{\gamma'}$ and the energy holding the electron to the orbital shell (the binding energy) E_B. Written as $E_e = E_{\gamma'} - E_B$; where $E_{\gamma'}$ is the partially energy from the total

$\gamma-$ray energy [22b][28]. The energy of the $\gamma-$ray after interaction can be written mathematically as follows:

$$E_{\gamma}^{'}=\frac{E_{\gamma}}{1+\left(E_{\gamma}/m_{e}c^{2}\right)\left(1-\cos\theta_{p}\right)} \qquad \{1.6\}$$

Here E_{γ} and $E_{\gamma}^{'}$ are the energy of photon before and after the scattering respectively, $m_{e}c^{2}$ is the rest mass of the electron and θ_{p} is the angle at which the $\gamma-$ray is scattered [28].

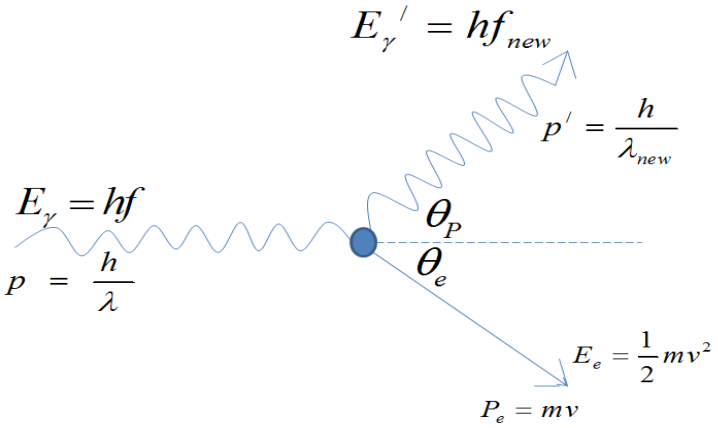

Figure 1.2: An illustration of the process of interaction of photon with electron (Compton scattering) *(Adapted from* [24a]*).*

1.5 Pair production

For $\gamma-$ray energies higher than 1.022MeV, the photon interacts with the nucleus of the absorber atom as it passes through it. In some instances interaction between an incoming photon and the nuclei will induce a creation of a positron-electron pair. This process will tend to take place in the vicinity of the nuclei, where the incoming photon will annihilate and a positron and an electron are produced in the process of the interaction. This process of interaction is called pair production. An excess energy above 1.022 MeV is distributed among the two particles produced as kinetic energy [22b].

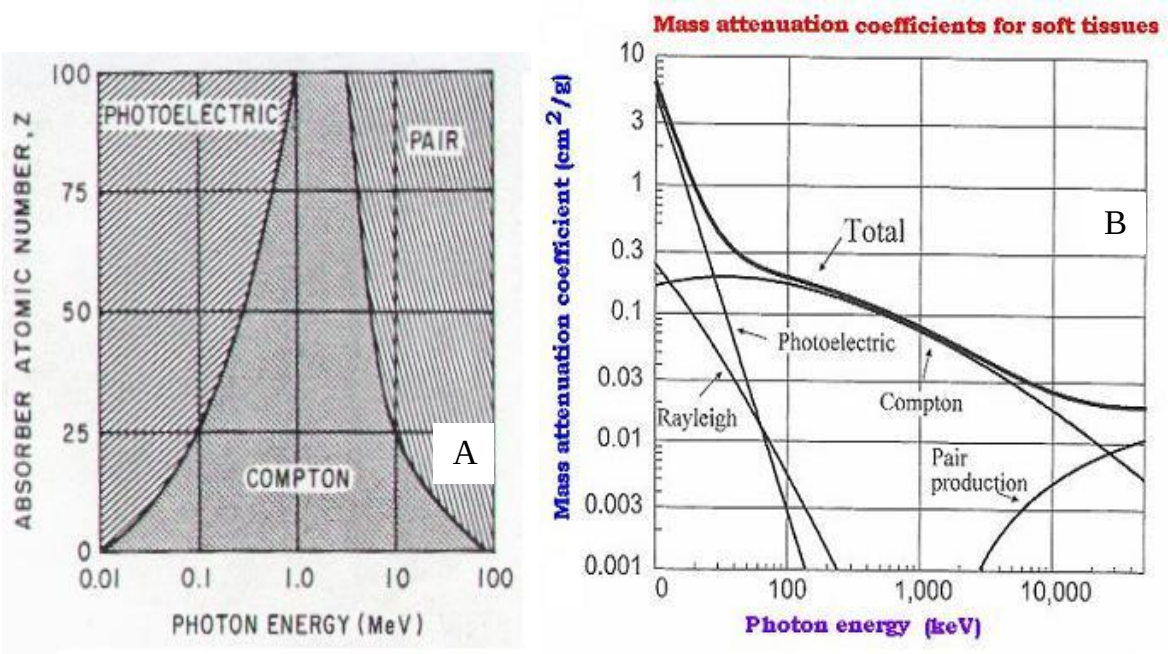

Figure 1.3: A) Linear attenuation coefficient and B) mass attenuation coefficient of γ rays of different energies in water (which is equivalent to the body tissue). Contributions of the photoelectric effect, Compton scattering and pair production are illustrated. *[Copied from* [30]*]*

Depending on the energy of the γ photons when passing through an absorbing medium (for example body tissue), one of- or a combination of the interaction processes (photoelectric effect, Compton scattering and pair production) described above may occur. The linear attenuation coefficient, μ is defined as the fraction of the incident γ photons that is either absorbed or scattered per unit thickness of the absorbing medium traversed [22b]. The mass attenuation coefficient is expressed as the linear attenuation coefficient divided by the density of the absorbing medium [30].

1.6 Production of Positron-emitters

In positron emission related nuclear medicine; the clinical goal is to make use of radioactive tracers, molecules with radio nuclides that are positron-emitters, with the purpose of diagnostic (medical) imaging of patients [3].

PET radiopharmaceuticals are made up of radio nuclides that are proton rich and decay by emitting β^+. The most commonly used PET radionuclides are ^{11}C, ^{15}O, ^{13}N, ^{18}F and ^{82}Rb, amongst these, F-18 FDG is the PET radionuclide used in this work. The standard way of producing F-18 FDG is by the use of a so called PET cyclotron. In a cyclotron, charged

particles (e.g. protons or negative ion, H^-) are accelerated in a circular path within (a) two D-shaped hollow metallic electrodes under vacuum [22c]. A General Electric PETtrace 6 cyclotron was used for the production of F-18 at the Centre of Nuclear Medicine/ PET at Haukeland University Hospital in Bergen, Norway. This PET cyclotron is capable of accelerating a proton to up to energy 16.5 MeV. These protons are thus accelerated to energies above the coulomb threshold, which is; the protons have energy above the energy barrier that enables p-n reactions to take place in interactions between the incoming protons and the target material. In the PETtrace 6 cyclotron, the protons are accelerated to the maximum energy of 16.5 MeV [22c], and steered into a target volume containing enriched water, H_2O (O-18). In the target, the nuclear p-n reactions p (O-18, F-18) n occurs, thereby producing an F-18 atom and an energetic neutron each time a p-n reaction occurs in the target material. The emission of en energetic neutron in each F-18 producing interaction dictates strict safety procedures and scales the radiation shielding requirements when producing PET isotopes with a cyclotron. The produced neutron field has a high intensity.

When enough F-18 FDG has been produced in the target volume at the cyclotron, the mixture of F-18 and H_2O (O-18) is transferred out of the cyclotron and further to the destination where the radioactive material is to be further processed (measured or synthesized), normally in a so-called lead shielded Hotcell. At this stage, in the Hotcell, the F-18 isotopes produced are separated from the target medium by a chemical method (such as distillation, chromatography and solvent extraction) [22c].

1.7 F-18 Fluorodeoxyglucose (FDG)

Fluorine 18 (F-18) is a fluorine radioactive isotope which is a source of positron with a half-life of about 110 minutes. The isotope is normally used in the radiopharmaceutical F-18 FDG (FluoroDeoxyGlucose), a widely used radiopharmaceutical in oncology, F-18 FDG source in cell division glucose which the human body will use as an energy source in cell division processes. When this radiopharmaceutical is injected in patients, it enables mapping of how glucose is utilized in the human body that is possible because the radiopharmaceutical is by acting as an analogue to glucose. The application of this radiopharmaceutical in imaging processes enables the imaging of malignant cancer [3]. In a hybrid PET/CT system, the use of F-18 FDG enables identification of the anatomic location of lesions (these will normally appear as hot spheres).

In this work water solution with F-18 was used instead of F-18 FDG. This is because there was easy access to F-18 than F-18 FDG. Also, given that this is a phantom study, the FDG part has less relevant for this experiment.

1.8 Clinical PET/CT protocols

PET/CT data acquisition protocols require a clinical PET and a clinical CT scan. In clinical studies, patients are positioned with their arms up in the scanner so as to reduce attenuation caused by the arms of patients in the field of view. For head and neck studies, the patients' arms are down during the image acquisition. The initial process in clinical PET/CT "study is the acquisition of a topogram", that lasts for 5.0 seconds. The range that both the PET and CT will scan on the topogram is defined according to particular indications for the ongoing study. That is from head to abdomen for head and neck cancer. According to [37], usually a slice thickness of about 5 mm is used to acquire a whole-body CT scan. However this slice thickness may not always agree with the standard protocol. A less than or equal to 3 mm slice thickness are normally preferred in cases such as head and neck scan. After the completion of the CT scan, the couch that the patient is lying on is moved to the PET field of view. "Over the same range as" that of the CT, a multi-bed PET scan is acquired in the PET field of view. In the event of acquiring the PET data, the CT images are reconstructed in parallel to the PET event. This permits attenuation and scatter corrections calculations to be performed in the process of acquiring the PET images. When the first bed position for the acquisition of PET images is completed, reconstruction of PET images commences [37].

The quality of reconstructed PET images is affected by some selected parameters. These selected parameters amongst others include the type of reconstruction algorithms, the type of filters, the image matrix sizes, and the correction methods. These parameters are briefly explained in Chapters 2 below. Also the combinations of these parameters that aid in reconstruction of PET images are tabulated in table 3.1 in Chapter 3.2 alongside the standard reconstruction parameters.

2. The Physics of an integrated PET/CT System

This chapter will introduce the CT and PET parts of the scanner related to this master thesis project. The physics of both scanners parts will be discussed, but most emphasis will be on the PET scanner. The integration of the two scanner part will be discussed in connection with reconstruction of PET/CT images.

2.1 The CT constituent of the PET/CT system

CT (Computed Tomography) scan, also known as X-ray CT or CAT (Computed Axial Tomography) scan, is a type of a medical imaging modality or procedure that employs X-rays. The name reflects that information is obtained from raw data that are computer-processed to create tomographic images or 'slices' in order to detect anatomical changes of specific areas of the body. These X-rays are generated from an X-ray tube [19][18c]. The CT is used in medicine as a diagnostic tool or used for screening of diseases such as cancer.

CT image quality is defined as the quality of being able to resolute (between details and noise) anatomy in an image. There are a number of factors that affect image quality in CT. In CT images, spatial resolution is the ability of differentiating between small objects that may be close to each other in the image. Some of the factors that affects spatial resolution (hence CT images) are pixel size, matrix size, and voxel size (Chapter 2.9.4), field of view (FOV), blur and slice thickness. The FOV is the factor that affects data in an image pixel. Thus, a decrease in FOV decreases the pixel size and hence the pixel contains less information. When the FOV is increased, the pixel size increases and more data from the patient are acquired. Also, thin slice thickness in general improves the resolution in an image [32].

CT images are also affected by the applied radiation dose. CT radiation dose is dependent on tube current-time (mAs), slice scan time and tube peak kilovoltage (kVp). mAs is the measured current at which the CT scanner is operated. The slice scan time is the time taken to obtain a single slice of an object; whiles the kVp is the energy of beam produced by the x-ray tube. When the mAs are increased, the radiation dose is "proportionally" increased. In this regard the expression for CT radiation dose is given by dose per mAs. Likewise, when the kVp is increased (keeping the other factors constant) subsequently the radiation energy is

increased. Since increasing the kVp results in more energetic beam, the (x-rays') beam particle's interaction length is increased. This makes it possible for the beam to penetrate throughout the patient and to reach the detectors outside the patient [33].

The CT scanner is used in combination with the PET scanner based upon two main reasons. The first reason is that accurate quantitative images of radiotracer concentration in an object cannot be obtained because reconstructing projection data directly from a PET scanner is not possible. Secondly, due to the attenuation of photons after annihilation of positrons, the CT part provides the attenuation correction of any photon that is detected [1][3][5][25].

2.2 The PET constituent of the PET/CT system

In vivo images are obtained according to the designed nature of PET scanners through the distribution and uptake of radiotracers on the fundaments of radio nuclides that emit positrons. This enables the study of body functions and enables a detection of changes in metabolic or biochemical processes that suggests diseases. When a positron interacts with an atomic electron, an annihilation process may occur, creating two 180° oppositely directed 511 keV photons to be emitted from the annihilation point [1]. The "back to back" annihilation photons produced as a result of positron interaction with an electron is detected by the PET detectors (Chapter 2.3) [18]. Also, the PET scanner is designed in a way that the patient or phantom to be imaged is surrounded by several scintillation detectors arranged in a ring around the patient [1]. These detectors (in PET) surrounding the subject imaged enable detection of photon pairs emitted from the subject in the detector ring [18].

Subsequently, the acquisition system records a photon hit with its location in a specific detector; the detector column and row identified (as described briefly in figure 2.1 below) denotes where the annihilation process occurred [3]. The radionuclide distributions obtained are used to acquire image projections as a consequence of the method of annihilation coincidence detection (ACD) of the PET scanner [1]. According to Richard and others (2008), the sensitivity and resolution is affected by the diameter of the ring of the PET scanner. This effect is due to angular sampling considerations. That is, the sensitivity and resolution are lower if the scintillation detector's ring diameter of the PET scanner is larger [2].

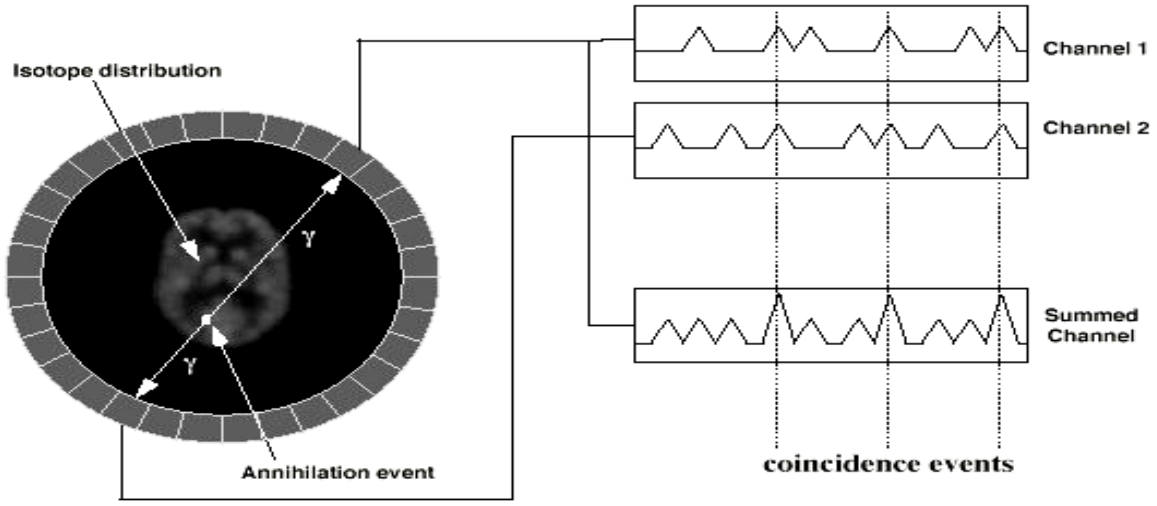

Figure 2.1: A diagram showing annihilation and detection process in PET scanners. Each detector generates a timed pulse when it registers an incident photon. These pulses are combined in coincidence circuitry, and are deemed to be coincident if they fall within a short time-window *(Copied from* [24]*)*

2.3 Detectors in PET

In as much as detection of signals is involved in the process of imaging, it is therefore of some benefit to explain the different types of detectors employed. Radiation detection involves the process of altering a type of signal detected to an alternative form of signal that can be observed and measured [20][25]. PET camera systems made of up to multiple rings of detectors are employed in PET imaging. These comprises of scintillation detectors (crystals) conjugated (linked) with photomultiplier tubes (a photo detector).

2.3.1 Scintillation Detectors

When there is an interaction between high-energy photons from a source with the atoms of a scintillation crystal, the electrons in the crystal are excited to a higher state, from its orbit or a valence band to a forbidden conduction band (that is not filled), of a higher energy state. When these atoms in the excited state quickly return to the ground state, they emit a visible light in a process called *luminescence*. The quantity of visible lights emitted by the crystal depends consequently on how many electrons are excited to a state of higher energy. Also, the amount of electrons excited is dependent on the incident photons energy. When this interaction occurs, the produced scintillation photons by the luminescence process are emitted in all directions from the point of interaction [1].

The most currently used scintillation crystal in clinical PET imaging are bismuth germinate, $Bi_4Ge_3O_{12}$ (BGO), lutetium oxyorthosilicate, Lu_2SiO_5 (LSO) and gadolinium oxyorthosilicate, Ga_2SiO_5 [1].

2.3.2 Photo Detectors

Photo detectors are applied in order to convert the signal from an electromagnetic shower produced from the traversing gamma rays, in the crystals of a scintillation detector, the scintillation photons, (3 – 4 eV) energy into an electrical signal that will be registered in the electronic data acquisition system belonging to the detector assembly. The efficiency of converting the incoming scintillation photons into an electrical signal is termed as a detector device's Quantum Efficiency [1].

Photo Multiplier Tubes:

Photo multiplier tubes (PMTs) are vacuum tubes consisting of i) a widow (which focuses the incoming incident photons), ii) photo cathodes which is followed by iii) several dynodes. A cathode is a negatively charged electrode and an electrode is an electrical conductor through which an electric current is passed. Each dynode (one of the series of the electrodes) is held at positions with a resistor chain having positive voltages bigger than the previous ones. As the incoming scintillation photons traverse into the photo cathodes as shown in figure 2.2, there is a release of photoelectrons in each dynode. For each dynode step, there is thus an amplification effect, where the initial signal is converted into a signal from more and more photoelectrons, thus producing a stronger electronic signal in the readout end of the PMT. As the photoelectrons are accelerated through subsequent dynodes with increasingly higher voltages; their number increases by a factor greater than 10^6. This creates a current at the anode in the range of milliampere [1].

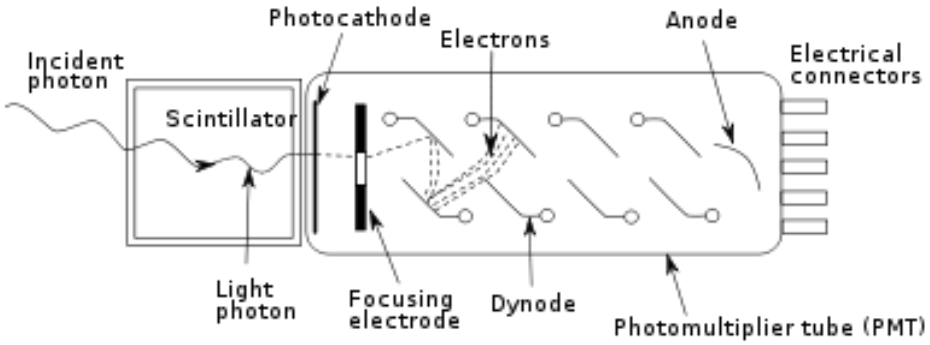

Figure 2.2: A schematic diagram of a photomultiplier tube.

The PET/CT scanner used in this master thesis work, a Siemens Biograph 40 PET/CT scanner, have high-speed ultra fast ceramic (UFC) detectors. Each detector element is allowed two projections readout, virtually simultaneously, which results in up to twice the number of detectors – slice acquisition [7].

2.4 Positron annihilation and coincidence detection

Annihilation process creates trajectories of the detected positron-electron paired photons known as LOR (line of response).

Coincidence detection is the process where after annihilation, the pair photons are detected by the ring of detectors. A *true coincidence* is the process whereby the interaction is simultaneously of a pair of photons as a result of the annihilation of the same positron-electron pair. A *random coincidence* is occurs when two different photons of energy 511 keV from separate annihilation process. The two photons occurred as a result of different atoms that decay and strike the opposite detectors simultaneously.

Another form of coincidence event, called *scatter coincidence,* is as a result when one or two of the 511 keV photons coming from a single annihilation process are scattered and are in turn detected simultaneously by the opposite detectors.

The total number of coincidence events (thus the number of, true, random and scatter events) detected by the ring of detectors in the PET scanner is known as *prompt coincidence* [1]. Apparently, these coincidence events are detected and the PET computer system records these events as a raw data set during the imaging period. For annihilation process occurring

deep inside the body, this coincidence event is less probable than for events occurring closer to the surface of the body [3].

During imaging, each photon detected along a LOR is recorded. Each point recorded on an image represents information obtained along a straight line path in each region through the patient. A set of points recorded along a straight line path is termed as projections (figure 2.4) [18][19]. When the intensity of the set of projections is displayed in a two-dimensional form, it is termed a sonogram [18].

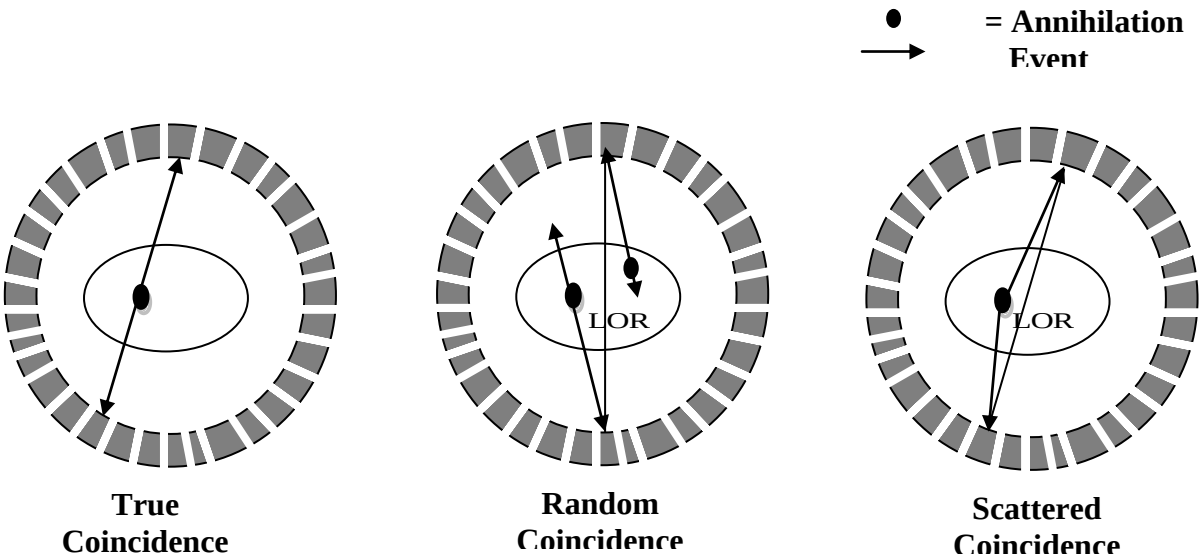

Figure 2.3: A diagram showing the different forms of coincidence detection. *(Adapted from* [24]*)*

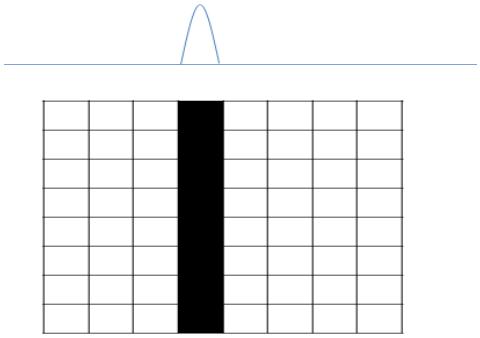

Figure 2.4: Illustration of a single projection from a detected photon. (*Adapted from [18]*)

Only the true coincidence counts were the type of event employed in the data analysis. Caramelo et al (2011) mentioned this in their work as a way to acquire a noiseless formation

of image [25]. The true coincidence counts were used in this thesis work. They are the pixel intensity values in the images. The mean of the pixels intensities within a particular sphere's ROI in Chapter 3.3 makes up the mean counts. The mean counts are therefore employed in the calculation of percentage contrast for each hot and cold sphere, percentage background variability, percentage relative error (accuracy of attenuation and scatter corrections) and standard deviations.

2.5 The integrated PET/CT system

The integrated PET/CT system is a combination (a so-called hybrid) of two well established medical diagnostic imaging technologies, the PET scanner and the CT scanner into a single medical imaging technology unit; the PET/CT scanner. The PET/CT systems enable physicians to identify cancerous cells or tumours or lesions, neurological diseases or heart disease [18c].

2.6 PET/CT quality assurance tests

QA (Quality Assurance) of an integrated PET/CT scanner pertains to the planned and systematic activities carried out in the hybrid system so as to fulfil the necessary quality requirements for high performance. Thus, the systematic measurement in comparison with a standardized monitoring procedure identifies the defaulted state of the integrated system if there is a default condition or state established.

A number of acceptable standardized procedures and tests are carried out daily on the integrated PET/CT system with both the PET and CT constituents of the hybrid being assessed for proper performance [2].

The CT daily check up is the first procedure performed at the start of the day after the restarting the computer. The steps involved in the daily check up before examination starts are the positioning of the CT quality phantom and the calibration of the patient couch position. The CT daily quality measurements are performed and these consist of the checking of three parameters on a water phantom. These includes the CT value of water (in Hounsfield units), the images pixel noise calculated as a standard deviation and the x-ray's tube voltage. These measurements are performed for all kV values available [38].

The daily quality check performed on the PET is maintenance procedure aims at the normalization of variations in the response of the many PET detectors. Based on the results produced, it is then known whether the system is ready for scanning or whether service needs to be undertaken on the system. The maintenance procedure performed includes verification and computation of the PET calibration factor. Using a phantom scan, a daily normalization results are displayed and the sonogram inspected. After the completion of the quality assurance procedures, the quality assurance results of the system are saved. At the operator's own discretion, partial detector setup can be performed [38]. The alignment between the PET and CT constituents is also checked as a part of the QA procedure. Some other tests performed on the PET scanner include count rate performance: prompt counts, true event (count) rates, random event (count) rates; accuracy of attenuation correction, accuracy of scatter correction and spatial resolution (quantitatively) among others [2][6][7].

2.7 Reconstruction of PET images

According to [1], the main goal governing the process of reconstruction of medical images is to provide an accurate cross-sectional image (and thus three dimensional volumes) of the distribution of radiotracers quantitatively. Secondly, the process of reconstruction is to provide (in vivo) the highest ratio of signal-to-noise [1].

2.8 Reconstruction Algorithms

In the evaluation of the quality of an acquired image, one has to define certain factors and apply to them some quantitative (objective) measures, with which, the quality of the acquired images can be measured. These factors are the different reconstruction parameters (reconstruction algorithm, filters, and matrix size, and attenuation and scatter corrections among others) used in the reconstruction process of the scanned data.

Although there are several different means of categorising reconstruction algorithms, PET reconstruction algorithms are mostly classified into two approaches: reconstruction by 1) filtered back projection and 2) iterative reconstruction [3].

2.8.1 Filtered Back Projection

Filtered back projection (FBP) basically is a method for reconstruction of medical images from their filtered projections. This method of reconstruction, as the name to some degree implies necessitates two principal steps:

i. Filtering the projection data and then

ii. Back projecting them so that reconstructed images is created [1][3].

During PET data acquisition, the images are acquired from natural forward-projections and then back projected, which is the direct opposite to the forward process. The process of acquisition of PET data is divided into sets of line integrals of a two (2) dimensional array of values from the object, which is transformed into a set of projections. While in back projection, this is the process of converting and distributing uniformly these set of projections to form a 2-Dimentional array (with data values) amongst the various pixels that fall in the projection path (figure 2.4 shows this process). When each back projected data set for all projections are summed up, the result is an approximation proportional to the radioactive distribution within a slice of the scanned object [18]. Nevertheless, when projecting a set of data back after forward projecting it does not necessarily yield the original object [3]. Statistical noise is one major limitation associated with the reconstruction of PET images using FBP. The extent of both noise and spatial resolution can be respectively reduced and maintained by appropriately applying a post reconstruction smoothing filter (such like Ramp, Butterworth, Hamming, Parzen, Shepp-Logan, Hann) [1][3].

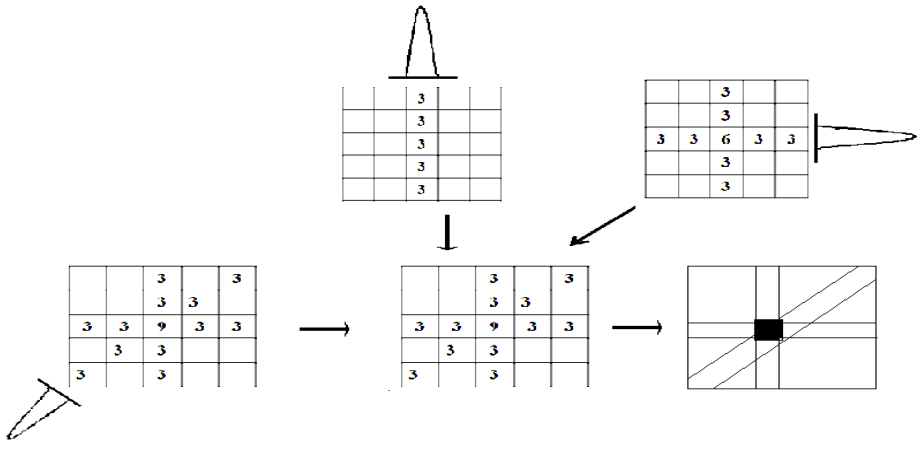

Figure 2.5: Schematic diagram of back projected data sets.

The filtering process (which is the initial process applied to the set of projected data before back projecting them) is done using an approach based on the Fourier Transform (FT). Fourier Transform is a way of representing a set of varying spatial data in the frequency domain. That is assuming there is a particular 1-Dimensional function *f(x)*, hence the Fourier transform is a representation of *f(x)* in the frequency space or domain. The function *f(x)* is described as having the sum of sine or cosine functions changing or altering frequencies (v_i) and magnitude, *F (v)* (where *v* is the frequency of the magnitude of the sinusoidal function *F (v)*). This estimate is written from Euler's equation as: $e^{i\theta} = \cos\theta + i\sin\theta$ (where $e^{i\theta}$ is a complex exponential) [18a]. When the function *F (v)* is transformed using the Fourier Transform, the resulting function created is the original *f(x)* and the transformation process from *F (v)* to *f(x)* is known as an inverse Fourier Transform.

According to Radon's work, if the Fourier Transform of the projection data is multiplied by frequency (*v*) and the inverse of Fourier Transform is then applied, the result produced is a filtered projection.

At this point, all data values are filtered of noise. When the filtered data set is back projected, it delivers somewhat the true object. Ramp filter is the most common filter used in frequency space [18].

2.8.2 Iterative Reconstruction

The iterative reconstruction algorithm depends on greater and more intense computational requirements than the FBP reconstruction algorithm. Moreover, in the reconstruction of images which have relatively poor counts, the iterative reconstruction algorithms are particularly useful [1][3]. In the reconstruction process, the iterative reconstruction method makes an initial estimation of activity distribution with regards to pixel values in the images. With this estimated distribution, a new estimation is acquired based on the counts from each forward projection. The original measured projection, in a so-called 'sinogram', a full representation of the projections in a 2-Dimensional form of matrix, $m_p(r,\theta)$ from the patient or object is then compared to the estimated counts of these series. The maximum likelihood is obtained from the comparison in the ratio: measured counts to estimated counts [1][3][18]. That is the maximum likelihood of the estimated counts matching the original measured counts. And based on the differences between these sinograms, it revises the

estimates. Until a result is obtained that is satisfactory, determined by a set of criteria for this, the iterations or process will continue. This method allows for modelling of the statistical noise. And finally to terminate the iteration processes, there must be an existing criteria associated with the algorithm that defines such a function [1][3]. From this account of maximum likelihood comparison, the iterations can continue for a long time in the attempt of the estimated counts matching the original measured counts. Each time the estimated counts are compared to the original measured counts, the difference is used to modify the estimated counts and the comparison is done again. The number of times a comparison is made is known as the number of iterations. The number of iterations can be huge as the estimated image data (to a maximum likelihood) is matched with the original measured image, and it is in general influenced by a generation of noise (figure 2.6). Thence, the appearance of noise in the resulting image limits the number of the iterations [18].

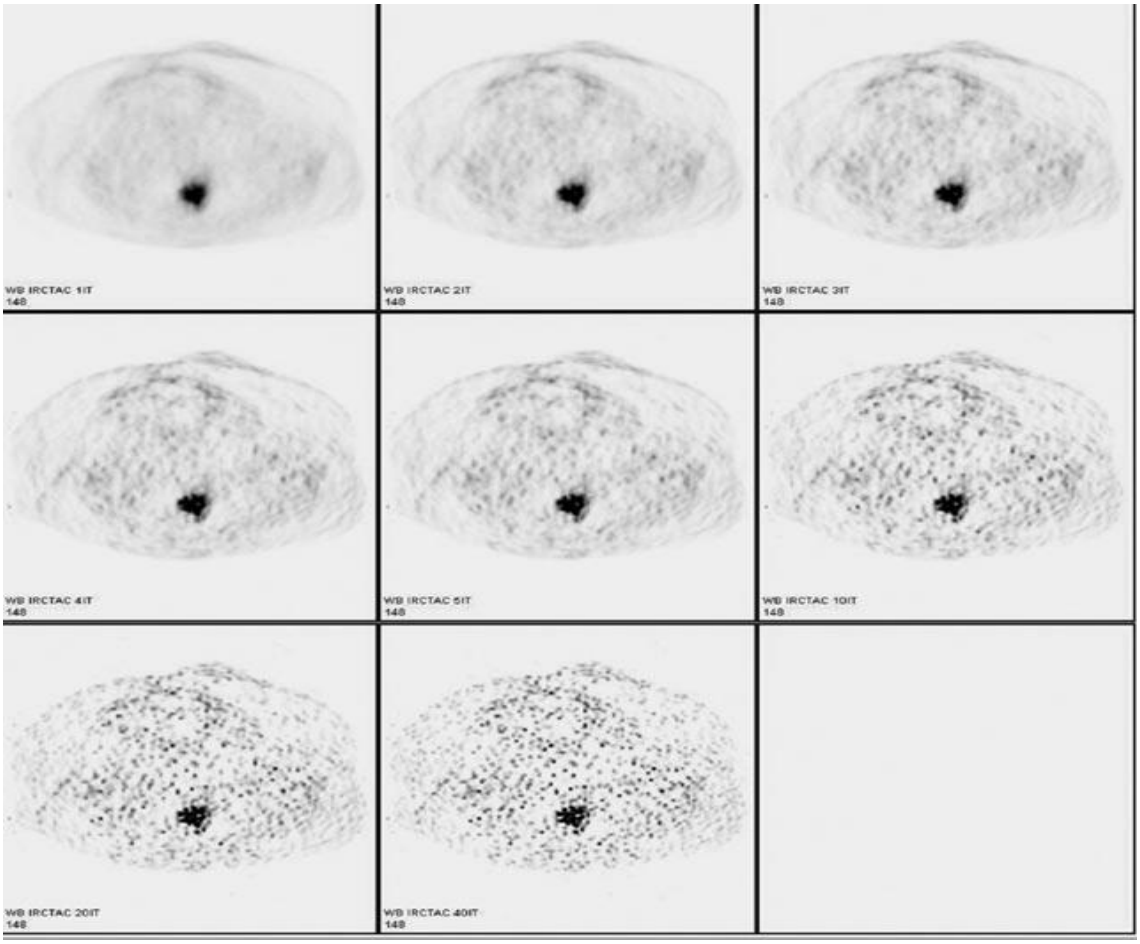

Figure 2.6: Illustration of how the number of iterations affects ovarian cancer images when all other factors are kept constant. The appearance of the image changes as the iteration increases from 1, 2, 3, 4, 5, 10, 20 and 40 (starting from the top left image to the last right middle image) respectively. *(Copied from [34])*

2.8.3 Subsets

Due to the extensive computational power required, the iterative reconstruction method is a slow method of reconstruction algorithm. There are various techniques implemented to improve the speed of the iterative reconstruction process. The ordered subset expectation maximization (OSEM) is one technique utilized to improve the speed of the reconstruction process [18]. In this technique, the projection sonograms are grouped in separate sets known as subsets. There are different ways with which this grouping can be made [15]. The projections grouped into subsets are each refined and updated to match the original measured image. Assuming there are sixteen projections (as shown in the schematic diagram 'a' below; figure 2.7), all the projections are not taken as a whole and compared, but rather smaller fractions of these projections are collected at a time and compared. In this example, the projections in the ring detector are divided into two (mirror-like) sets of 180-degrees. The projections that fall under a particular angel of similar value are considered to be in a specified group. After grouping them, the result is as shown in the sets, 'b'.

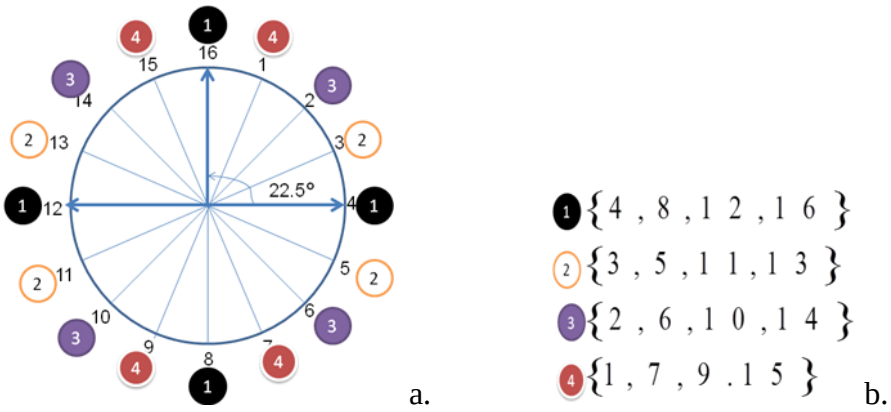

a. b.

Figure 2.7: An aggregate of 16 projections ('a') divided into 4 subsets ('b').

As the number of subsets speeds up the maximization process of approaching the true measured counts. In an approximation, the number (N) of subsets generated increase the speed up process to about N times the maximum likelihoodness [15].

2.9 Image Corrections

An uncorrected image (in terms of attenuation and scatter) looks coarse and somewhat noisy (contains gravel-like dots in it); thereby making identification of smaller detailed objects

difficult. In this section, attenuation and scatter corrections will be discussed. How they affect the image after reconstruction will also be presented.

Attenuation

Reconstruction of the raw projection data are not acquired directly from a PET scanner in order to obtain accurate quantitative images of the radiotracer concentration in the object (NEMA IEC body phantom). Projections prior to reconstruction process needs to undergo several corrections so as to guarantee optimal quantification. As much as attenuation is put into the reconstruction algorithm, it is also required and important that these corrections are applied [1][5].

When a measured beam of photons with initial intensity I_o, encounters a medium of particular thickness, x, some of the incoming photons will interact with the atoms of the medium and some photons will pass through. The interaction removes some of the photons from the initial beam and the rest continues through the medium with intensity I_x. This process of reducing (through absorption and scatter) the intensity of an initial beam of photons is generally known as *attenuation*. The beam of photons is said to be attenuated as it passes through matter [1][5][25].

One aspect of imaging with PET is that for annihilation of positrons taking place at any point along the ray, a attenuation correction parameter is the same with regards to whatever given projection of the ray (equation {2.1}) [3]. Mathematically, a parallel beam of radiation photons undergoes exponential attenuation as it passes through a medium.

Since attenuation and scatter are manifestations of the physical processes that take place when photons traverse through matter [1], correction for both is important.

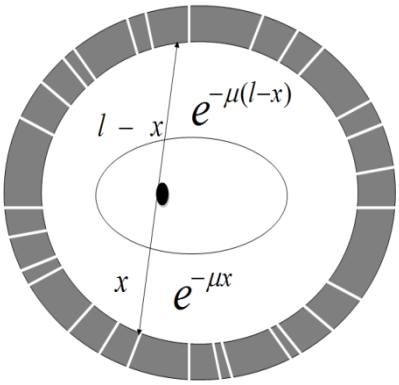

Figure 2.8: A diagram showing attenuations as the two photons move to the detectors.

2.9.1 Attenuation Correction

The attenuation correction is based on the probability that the two photons would reach the detectors simultaneously. Looking at the below equation, {2.1}, the first photon reaches the detector at *x* distance and with a probability of $e^{-\mu x}$ and the second photon reaches the opposite detector at a distance *l-x* and with a probability of $e^{-\mu(l-x)}$ [3]. Mathematically, the attenuation correction is the multiplication of the two probabilities with which the two photons reaches the detectors.

$$I_x = I_o e^{-\mu x} \quad ; \quad I_{l-x} = I_o e^{-\mu(l-x)} \qquad \{2.1\}$$

where μ is the linear attenuation coefficient for 511 keV photons in tissues

Thus,

$$AC = e^{-\mu x} \times e^{-\mu(l-x)} \quad \Rightarrow \quad AC = e^{-\mu l} \qquad \{2.2\}$$

Where: *AC* – Attenuation Correction; μ - Linear attenuation coefficient; l - Total path length between two opposite detectors.

Hence the attenuation parameter is the same no matter the projection ray due to the fact that the total length is considered rather than the individual distances. According to Robert Koeppe (2009), the attenuation correction can be written as $e^{+\mu l}$ [3]. From the above equation {2.2}, it is difficult to obtain the correct attenuation correction. The reason is that, there are different projection rays with different lengths (l) and linear attenuation coefficient

(μ) and since the correction has to be done on each ray projected. This problem is somewhat solved when each pixel in the overall image is segmented and by specifying an attenuation coefficient for each pixel from a transmission scan based on the segmentations. The pixels (image) segmented in practical applications are smoothed. Thus a transmission scan is performed on the PET scanner and the transmitted signal is measured. This is done by rotating one or more sources around the patient. Since the strength of the source is unknown for the PET scanner system, the line integrals of the LOR are determined with an empty gantry by performing a blank scan [37]. The pixels are then used to compute or estimate the attenuation factor (Equation {2.3}) according to the emission data. Propagation of noise from the transmission measurements is reduced to a greater extent in this process into the emission images reconstructed.

$$A_{i,j} = \frac{Blank_{i,j}}{Trans_{i,j}} \qquad \{2.3\}$$

Where $A_{i,j}$ - the Attenuation correction factor; $Blank_{i,j}$ and $Trans_{i,j}$ represents the counts recorded in the scans of both blank and transmission for the pair of detectors.

2.9.2 Scatter Correction

During a Compton scattering, the after interaction products are a photon with an amount of energy and the recoil electron with a certain amount of energy. When the scattered photons from Compton events are detected, they form scattered coincidence. The annihilation photons on the other hand form true coincidence. There are different techniques to correct for the scattered photons. One approach by which the correction can be derived is to utilise the data from the original image contaminated with scattered photons and the transmission image. From the emission image, activity distributions in the body are indicated [18c]. Whereas images from the transmission scan indicates the tissues' attenuation coefficient. With the use of a computer design to model, the scattered events distributions can be derived from the interaction of photons and the two images acquired. Thus, an estimation of the scattered events distributions is applied. Also how the scattered events relate to each data profile can be derived. The result from this estimation is then deducted from the projection data. Finally, the reconstruction of the newly formed image data from the deduction is repeated until a preferable image data is attained [18c][25].

2.10 Filters and kernels

Filters and kernels are techniques used to reduce or remove noise from an image.

Kernels employed in CT imaging are used together with numbers to define the sharpness of the image. Higher (increased) numbers represent sharper images and lower (reduced) numbers represent smoother images [7].

There were a number of predefined filters associated with the PET scanner for image reconstruction. The PET filters available in the Siemens Biograph PET/CT scanner system are: All pass, Box car, Butter worth, Gaussian, Hamming, Hann, Median, Parzen, and Shepp filter.

Filtering of PET images

Filtering can be done in two domains namely:

i. Spatial filtering domain

ii. Frequency filtering domain

Spatial Filtering is the mechanism of moving mask from pixel to pixel or point to point in an image. A predefined relationship or function is used to calculate the response at that point received (responded) by the filter [12].

Smoothing (spatial) filters are employed for the purpose of blurring and for noise reduction. In pre-processing steps, blurring is employed for removal of small detailed noise prior to extraction of large objects in an image and joining together small curves or line-gaps [12].

In the frequency domain, the spatial image is converted first into a frequency image domain. The Fourier Transform is used in the conversion process [12]. Frequency filters can be grouped into three types, namely: Low pass filters, high pass filters [17] and band pass filters (which are not so frequently used). Hence discussions would be made on only the low pass and high pass filters.

Low Pass Filters (LPF)

These are filters used that enables low frequencies to pass through and reduces (attenuates) the passage of high frequencies. They cut off components of the Fourier Transform with high frequencies at a distance from the origin of the transform greater than a specified distance from the same origin [12].

High Pass Filters (HPF)

These are filters used to attenuate the passage of low frequencies and enable high frequencies through it. It is also utilized in the enhancement of edges or small image objects. It best fits the preservation of high resolutions at the expense of statistical fluctuations counts of high degree [12].

Filters in general can either be linear (e.g. Gaussian filter) or non-linear (e.g. median filter) to blur the image for the purpose of reducing noise. The Gaussian filter can be used as either HPF or LPF.

2.10.1 Convolution of PET images

Convolution means the mathematical way of creating a single array of values from the product of two different arrays of values having dissimilar sizes but similar dimensionality. In other words, it is the combination of two separate signals to form a third single signal. [16] The final single array also has the same dimensionality.

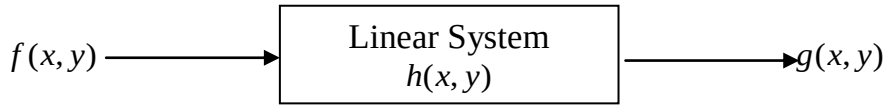

$$f(x,y) \otimes h(x,y) \Rightarrow g(x,y)$$

Where $f(x,y)$ - The image data

$h(x,y)$ or $\otimes$ - The convolution linear system

$g(x,y)$ - The resultant image produced

Using a data matrix, the convolution process is shown below.

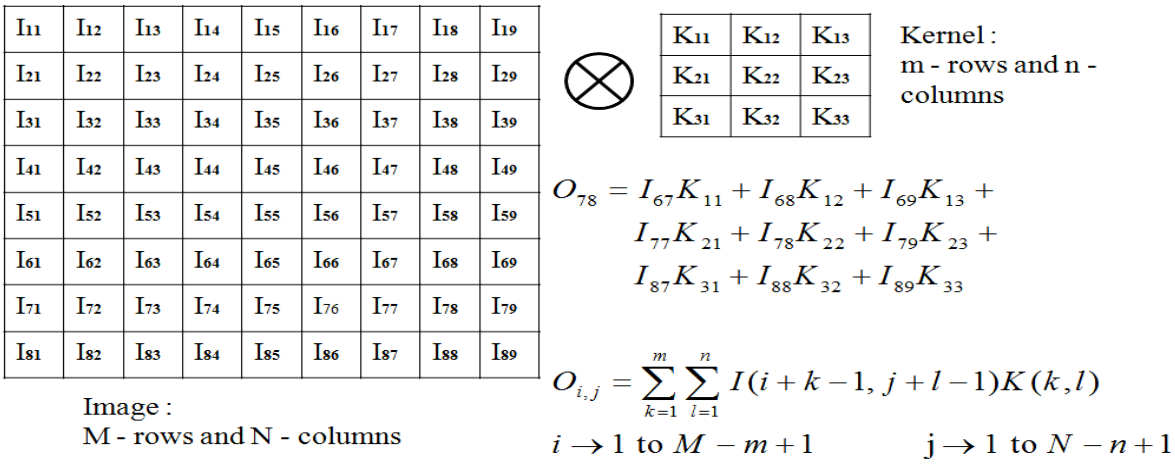

Figure 2.9: An example of how a convolution is carried out. *(Adapted from [25])*

2.10.2 Gaussian Filter

A very significant filter is the Gaussian filters. The reason is based on its theoretical and practical use. It is a linear convolution filter. Gaussian filter is applied in a different way to that of the mean filter (each pixel value is divided by the total sum of weight of the entire pixel in the filter) and it has the ability of smoothing the image. It has a simple Gaussian function with a degree of one (thus 1-Dimension consisting of normally only the x - axis). But it can also be mathematically written as a 2-Dimensional discrete approximation to the below continuous function assigned with two free parameters:

I. The kernel size *(N x M* filter mask*)* desired

II. The standard deviation's value, σ of the Gaussian function

$$G(x,y) = \frac{1}{2\pi\sigma^2} e^{-\frac{x^2+y^2}{2\sigma^2}} \qquad \{2.4\}$$

Where: σ - Standard deviation of the distribution

x - Horizontal component of the distribution

y - Vertical component of the distribution

Working with the above 2-Dimensional Gaussian equation directly sometimes seems to slow the process of filtering. Therefore separating it to form a two 1-Dimentional Gaussian function makes implementation faster and quicker. The two separable variables associated with the Gaussian distribution means first filtering or convoluting with a vertical ('y direction') component and then followed by filtering or convoluting the result with a horizontal ('x direction') component. Multiplying the two separate components yields the 2-Dimentional equation above. This idea is termed separation of variables.

$$G(x) = \frac{1}{\sqrt{2\pi}\sigma} e^{-\frac{x^2}{2\sigma^2}} \text{ -------- } x \text{ direction}$$

$$G(y) = \frac{1}{\sqrt{2\pi}\sigma} e^{-\frac{y^2}{2\sigma^2}} \text{ -------- } y \text{ direction}$$

$$G(x) \times G(y) = G(x, y) = \frac{1}{2\pi\sigma^2} e^{-\frac{x^2+y^2}{2\sigma^2}} \qquad \{2.5\}$$

Looking at it using a kernel matrix of size 3x3, can be separated as follows:

1	2	1
2	4	2
1	2	1

=

1
2
1

×

1	2	1

Figure 2.10: A 3x3 matrix showing a Gaussian kernel separable variables.

Below is an example of the application of the Gaussian kernel. Example 2.1:

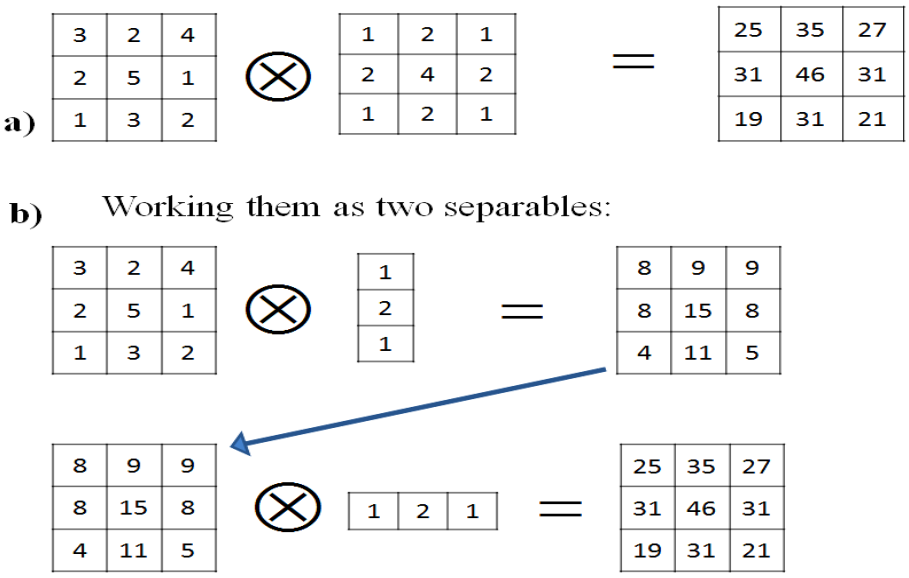

Figure 2.11: a) A 3x3 image matrix convolved with a 3x3 Gaussian kernel. b) The same 3x3 image matrix convolved with a Gaussian kernel separable variables. The image matrix was first convolved with the vertical variable and the result was convolved with the horizontal variable.

Initially; the parameter of the standard deviation, σ controls the degree of smoothing in the image. It is however not controlled by the absolute value of the size of the kernel. The standard deviation, σ is normally user defined. Secondly, the Fourier Transform, which is a Gaussian function, makes it rather have a special property. This enables analysing with the filter in the spatial frequency domain very convenient. According to Chris and Toby (2001), it is commonly used as the initial stage algorithm for edge detection (where impulse response is a Gaussian function) [10].

2.10.3 Full Width at Half-Maximum

From the Gaussian distribution equation stated above, the standard deviation which determines the degree of image smoothing is represented as half the width of the distribution (which is located at 60% of the height of the distribution). Nevertheless, in most applications, the Full Width at Half-Maximum (FWHM) is rather employed though it may be bigger than the standard deviation, σ itself. To compare the impact of FWHM on reconstructed images, FWHMs of 3, 4, 5, 6, 7, and 8 mm were used. The FWHM can be derived as follows:

$$FWHM = 2\sigma\sqrt{2In2} \qquad \{2.6\}$$

$$FWHM = 2.354\sigma \quad \text{(mm)}$$

Therefore, from the chosen FWHMs the values were attained with different values of σ (shown below).

$$\sigma = \frac{FWHM}{2.354} \qquad \{2.7\}$$

The unit of the FWHM used in this work is millimetres (mm). For a normal Gaussian distribution (assuming mean, μ is zero), σ is taken to be one (1). As the standard deviation, σ increases, the wider the width of the Gaussian distribution curve. And this in turn increases the value of the FWHM. This factor makes the image smoother. And the further σ is increased; the image appears to be more blurred.

2.10.4 Median Filters

Median filter is an example of an ordered statistical filter. They are non-linear spatial filters. The response of a median filter is based on arranging the pixels contained in the image areas within the filter. The value determined at the centre pixel is replaced by the median filter as the result [12],[20]. Median filters are capable of reducing certain kinds of random noise with substantially less blurring in the image than linear spatial filters having the same size [12].

In median filtering, a pixel within the image is addressed (convoluted) and its (*N x M)* neighbourhood is replaced by the statistical median. The median filter is a good filter in the sense that it preserves details (edges) with high frequencies and at the same time removes noise, particularly noise spikes which are isolated [10]. Median can also simply be defined as the middle element. The median *m*, therefore, of a set of numbers is the number positioned in the middle of the set of numbers such that half of the numbers are on each side of *m*. Meaning, half of the numbers are less than the median number *m* and half of the numbers are greater than *m*. It is always the middle (midpoint) element or number of a sorted set of elements or numbers (distribution) [17].

Thus the median operator requires that the data or values within a pixel neighbourhood are first rearranged or ordered at every pixel location [17]. The explanations given here are for *odd* numbers of elements. For *even* numbers of elements, the middle two numbers are summed up and then divided by two (2).

Example of even *4x4* neighbourhoods: 22 20 25 50 123 100 200 30

The median is 20 22 25 **30** **50** 100 123 200

$$\left(\frac{30+50}{2}\right)=40$$

Using an image matrix, the median is done as follows.

Example 2.2:

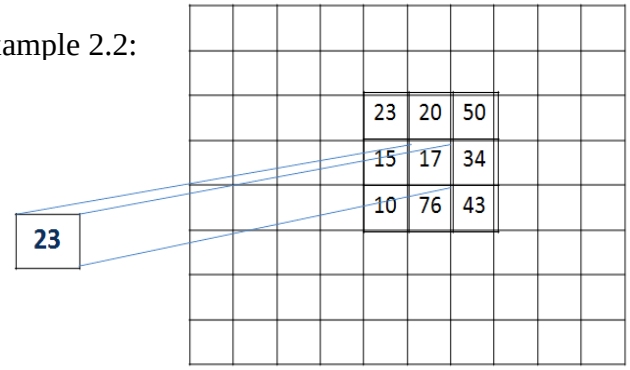

23 20 50 15 17 34
10 76 43

Re-arranging:
10 15 17 20 **23** 34
43 50 76

Median = 23

Exaple 2:
Using a 1D kernel

8	7	3	**2**	**6**	**5**	9	3	4	7	5	6

Result:

7	3	3	**5**	6	5	4	4	5	6

Let's define the 1-Dimensional median kernel to be of 1x3 matrix size. Below are the process followed in obtaining the results.

8	7	3	= 3, 7, 8 = 7

6	5	9	= 5, 6, 9 = 6

3	4	7	= 3, 4, 7 = 4

7	3	2	= 2, 3, 7 = 3

5	9	3	= 3, 5, 9 = 5

4	7	5	= 4, 5, 7 = 5

3	2	6	= 2, 3, 6 = 3

9	3	4	= 3, 4, 9 = 4

7	5	6	= 5, 6, 7 = 6

2	6	5	= 2, 5, 6 = 5

2.10.5 Hann Filter

Hann filter is a low-pass type filter. The magnitude of the Hann filter is written as follows:

$$h(f) = 0.5 + 0.5\cos\left(\frac{\pi f}{f_K}\right); \quad |f| < f_K \qquad \{2.8\}$$

Where f – Spatial frequency of the image and f_K - Cut-off frequency. The cut-off frequency serves as a boundary or limit in a system's frequency response region, where frequencies passing through are attenuated based on a specified magnitude of the cut-off. Hence, Hann filter cut-off frequency allows all frequencies that are less than the cut-off frequency magnitude to pass through and thus cut off all higher frequencies. Hann filters are often used in studies where accurate statistics are highly needed with regards to loss in spatial frequency. This is because the Hann filter sets all frequencies above the cut-off frequency quickly to zero and thus making it a very good smoothing filter [20].

In practice, the kernel or filter incorporates the Hann filter function and hence the cut-off frequency. But the basic knowledge behind that principle is that assuming the kernel has a particular cut-off frequency, at every pixel, the corresponding frequency value is set in the equation function and the result yields a new value for the central pixel (as explained in the principle of convolution above). However, the value of the cut-off frequency (and that of the critical frequency) was not user selected in the scanner system.

Emaple 2.3:

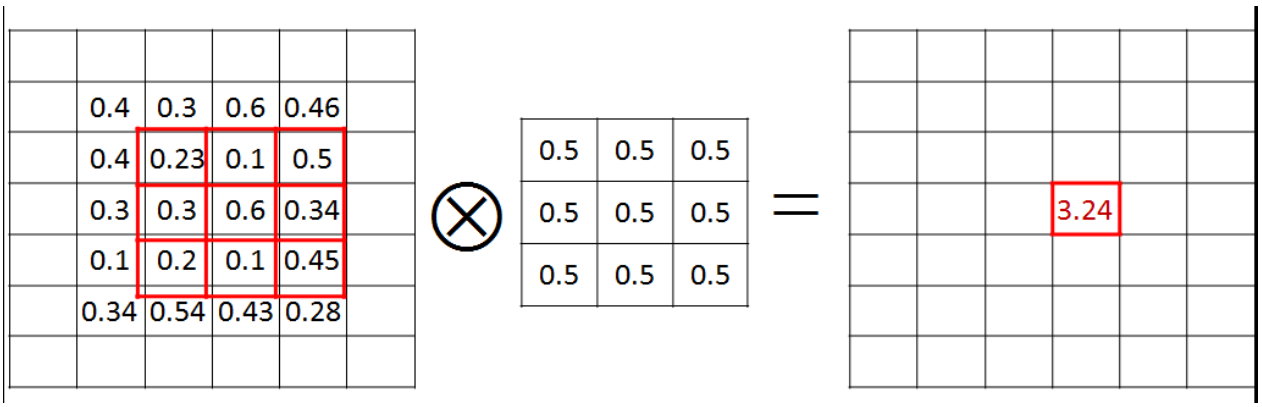

Figure 2.12: A diagram showing how the Hann filter is used to convolve an image.

Example 2.4:

$$h(f_1) = 0.5 + 0.5\cos\left(\frac{0.23\pi}{0.5}\right) = 0.562$$

$$h(f_2) = 0.5 + 0.5\cos\left(\frac{0.46\pi}{0.5}\right) = 0.015$$

$$h(f_3) = 0.5 + 0.5\cos\left(\frac{0.50\pi}{0.5}\right) = 0.000$$

From the above example, the Hann filter fucntion was employed in the convolution process. In this example, each pixel frequency in the 7x7 image matrix was first converted using the Hann filter function. The central position pixel frequency (of 0.6) in the image was then replaced by the total central pixel value (3.24) of the convolution result. To observe what happens in each pixel frequency conversion, a worked example of some selected pixel frequencies are shown above. Looking at the result of each pixel frequency converted, it was found that the image pixel frequency that is less than the cut-off frequency yields a resulting value of non-zero decimals. However, in the case of image pixel frequencies approaching or higher than the cut-off frequency, the result attained approaches zero (0) and or exactly zero.

2.10.6 Butterworth filter

Another low-pass filter is the butter worth filter. Mathematically, it is represented by the equation {2.9} below. The equation or filter function is made up of two parameters; the critical frequency, f_C and the power, p (also referred as the order, n). Where: $p = 2n$.

The magnitude of butter worth filter,

$$b(f) = \frac{1}{\sqrt{1 + \left(\frac{f}{f_C}\right)^{2n}}} \qquad \{2.9\}$$

These parameters describe the operation of the filter. The order is related to how fast or speedily the Butterworth filter is rolled-off. It is needed for studies where the preservation of higher resolution is required with regards to high fluctuations in the statistical counts.

According to [22a], the image is more smoothen when the order in maintained and the critical frequency is lowered [22].

In Butterworth filter function, [20] argued that the cut-off frequency was not used as in the case of the Hann filter function. Rather the critical frequency was used in that regard. It was further explained that the Butterworth filter at a certain point begins to "roll-off" approaching (or towards) zero (0). The critical frequency is hence that point reached instead of being the point at which the "roll-off" determined as zero (0). Thus, the Butterworth filter certainly does not reach zero, rather it approaches zero [20]. The critical frequency of a Butterworth filter was not user selected (in the Siemens PET/CT scanner) and is therefore predefined in the scanner system [22a]. It is also found to be the cycles per pixels or cycles per centimetre of image $(cycles/pixel$ or $cycles/cm)$ [20].

From the above example (2.4), equation {2.9} of the Butterworth filter in a way can be constructed to imitate that of the Hann filter [20]. Hence from worked examples (not shown in this work), it was also observed that an increasing image pixel frequency approaching or higher than the critical frequency results in a value approaching zero. Regardless of this process, the resulting value from the Butterworth filter function gradually approaches zero unlike the Hann filter function. Example; frequencies of 0.43, 0.78, 20, 50 and 80 convolved with a critical frequency of 0.5 $cycles/pixel$ and an order of one (1) results in new pixel values of 0.752, 0.540, 0.023, 0.010 and 0.006 respectively. Using the same image pixel frequencies and critical frequency, when an order of ten (10) was used, the resulting values are 0.976, 0.012, 0.000, 0.000 and 0.000.

In the Siemens Biograph PET/CT scanner system employed in this work, the system allows for the selection of the order of the Butterworth filter (which have values: 1, 2, 3, 5, 7, 10 and 20). In a manner of comparing the effect or quality of reconstructed images, different orders; 1, 10 and 20, were applied in the reconstruction with Butterworth filter.

2.11 Image matrix size

Images are created when raw data are segmented in very small parts. A grid that is made up of very small squares of rows and columns is known as a matrix. Each square in the image matrix is known as a pixel. The size of the matrix denotes the number of pixels contained in

the grid. For example a 128 matrix used in this project work to reconstruct the PET images had 128 pixels along the row and 128 pixels along the column. The grid has a constant perimeter; therefore a bigger matrix size (256 x 256 pixels) will have its individual pixels to be smaller than that of the 128 matrix size. Therefore, matrix size controls pixel size.

Each pixel contains a detail of the patient imaged. The detail in each pixel represents the information recorded as x-rays traverses that region of the patient and hits a detector. A bigger pixel size contains more details than a smaller pixel size. Hence, each bigger pixel will have different densities within which is less likely to occur in smaller pixel sizes. For this reason, smaller pixel sizes improve spatial resolution. Again, as matrix size determines pixel size, it can however be stated that matrix size have an effect on spatial resolution [32].

3. The Measurements and Data Analysis

3.0 Set up and equipment

The applications of the NEMA IEC phantom includes simulation of whole-body imaging especially using PET and camera-based coincidence imaging techniques, evaluation of reconstructed image quality in whole body PET and camera-based coincidence imaging and determination of the coincidence count rate characteristics in brain and cardiac imaging. It is also applied to evaluate the relationship between true coincidence count rate and radioactivity, to determine the address errors caused by address pile up and to evaluate the count loss correction scheme.

Main Features:

The NEMA IEC Body Phantom Set™ (Model PET/IEC-BODY/P) consists of the following features

i. Body phantom

ii. A cylindrical lung insert, filled partly with low atomic number material with an average density of 0.30 ± 0.10 g/cc

iii. An insert with six fill-able spheres (compartments) with various sizes. Two large spheres with internal diameters of 28 and 37 mm and four small spheres with internal diameters of 10, 13, 17 and 22 mm.

iv. A line source contained in a test phantom (a solid polyethylene cylinder)

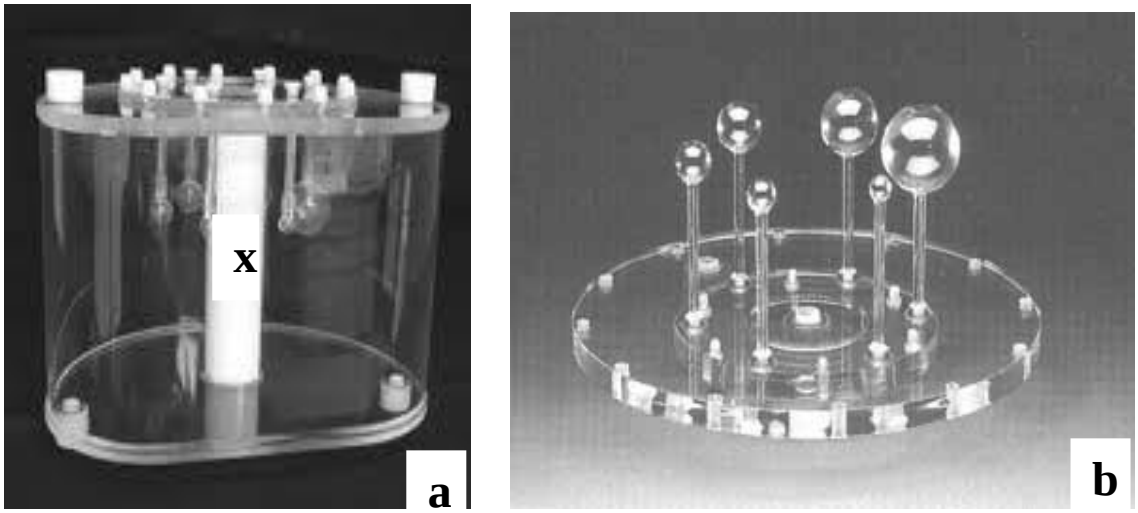

Figure 3.1: (a) NEMA IEC Body Phantom Set™ (b) Lid cover with six fillable spheres. The position marked 'X' is the lung insert filled with polystyrene beads and water.

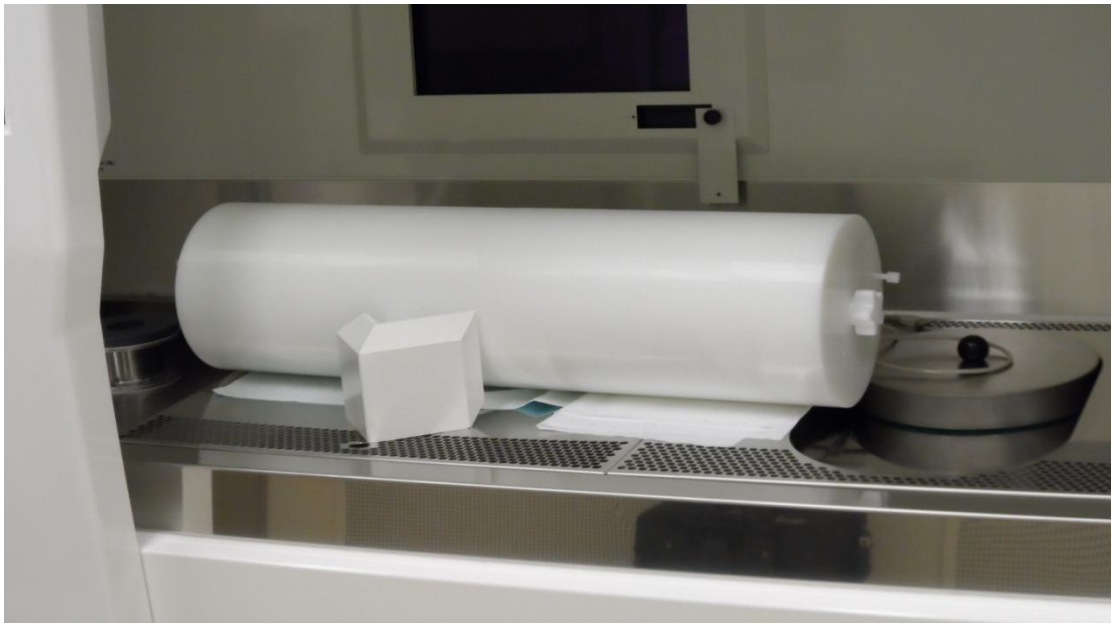

Figure 3.2: Scanner extension phantom. This was used to stimulate radiation that extends beyond the scanner.

The phantom is designed in accordance with the International Electrotechnical Commission (IEC) recommendations and the modification was done by the National Electrical manufacturers Association (NEMA). Its use is recommended for the evaluation of reconstructed image quality in whole body PET imaging

3.1 Experimental procedure

The four parts of the NEMA IEC imaging phantom was filled with either activity or non-radioactive water. Below are the descriptions of how each compartment was filled.

3.8.1 Filling the lung insert

The lung insert is made up of a cylinder that is mounted in the centre of the torso cavity. The lung insert is filled with polystyrene beads (low density material) and non-radioactive water was then injected into it. This was done to simulate lung density. According to [6], the "NEMA Standards Publication NU 2-2001, section 7.3.3", the lung insert was required to have an average density of 0.30 ± 0.10 g/cc (0.286 g/cc was measured: 40.1 g; volume of water:110 cc and total volume of lung insert: 136.0 cc). The lung insert was used in order to measure the residual error due to scatter and attenuation corrections.

3.1.2 Filling the body

Initially, the torso cavity (representing background) was filled half way through, about 4.8 litres, with non-radioactive water only. This was done with the lung insert (filled with non-radioactive water and low density atomic number material) in position. The lid with spheres connected or screwed to their positions was afterwards securely placed on top to hold the lung insert in its position and to cover the torso as well. F-18 was used as the radioactive material in this work. An amount of F-18 was measured with a catheter-tip type 20 ml syringe; such that the concentration of the activity measured together with non-radioactive water (a total volume of 9.708 litres) will be 5.3 kBq/cc (0.14 μCi/cc) at the time of scan. This activity concentration corresponds to 370 MBq (10 mCi) per 70,000 cc, a typical injected dose for a standard adult patient undergoing a whole-body PET/CT examination. The F-18 measured was flushed into the half-filled non-radioactive water in the background. The syringe was flushed several times to ensure the transfer of almost all F-18 out of the syringe. After injecting the measured activity into the torso cavity, the mixture was stirred carefully and gently. The remaining water was then added to the solution or mixture in order to achieve the total quantity of 9.708 litres. To ensure thorough and even mixture of the activity and water, a long solid plastic was used to stir the concentration for some time. Placed in a well shielded hot cell, it was allowed to settle.

3.1.3 Filling the six spheres

The two large spheres (28 mm and 37 mm) were filled with non-radioactive water to simulate cold lesion imaging. A catheter-tip type 20 ml syringe was used to prepare an activity concentration (with a total volume of 9.98 ml for the 4 small spheres). This volume would contain an activity that would be 4 or 8 times respectively to the level of activity concentration in the volume representing the background. By putting the catheter-tip of the syringe through the removed filler cap opening with a narrow tube (stem) from the outer side of the lid, the syringe with activity concentration was injected into each of the four small spheres (10, 13, 17, and 22 mm).

When all the spheres and background including the lung has been filled, the phantom was tilted to ensure that there was almost no air inside. Air bubbles could interfere with the measurement of contrast recovery.

3.1.4 Filling the scanner extension phantom

In filling the test phantom (line source in the solid polyethylene cylinder), a measure amount of 5.6 ml of the same activity concentration used in the torso cavity was carefully injected through the narrow hole line source by applying a simply pressure technique. This was done to have activity that extends beyond the scanner as in clinical situation.

3.1.5 Scanning the prepared phantom

The prepared NEMA IEC body phantom (body, spheres and test phantom compartments) filled with sphere-to-background ratio of either 8:1 or 4:1 were scanned with a standard clinical whole body PET/CT protocol on a Siemens Biograph 40 PET/CT scanner (Chapter 3.2). The phantom was placed on the imaging table and positioned axially in the scanner in a way that the centre of the spheres was at the middle slice of the scanner. The test phantom was placed at the head end of the body phantom and adjacent to the body phantom (figure 3.3). The B19f (B: body) very smooth kernel (Chapter 2.10) was used in the CT imaging process.

Three repetitive experiments following Chapters 3.1.1 to 3.1.5 were done for each concentration ratio.

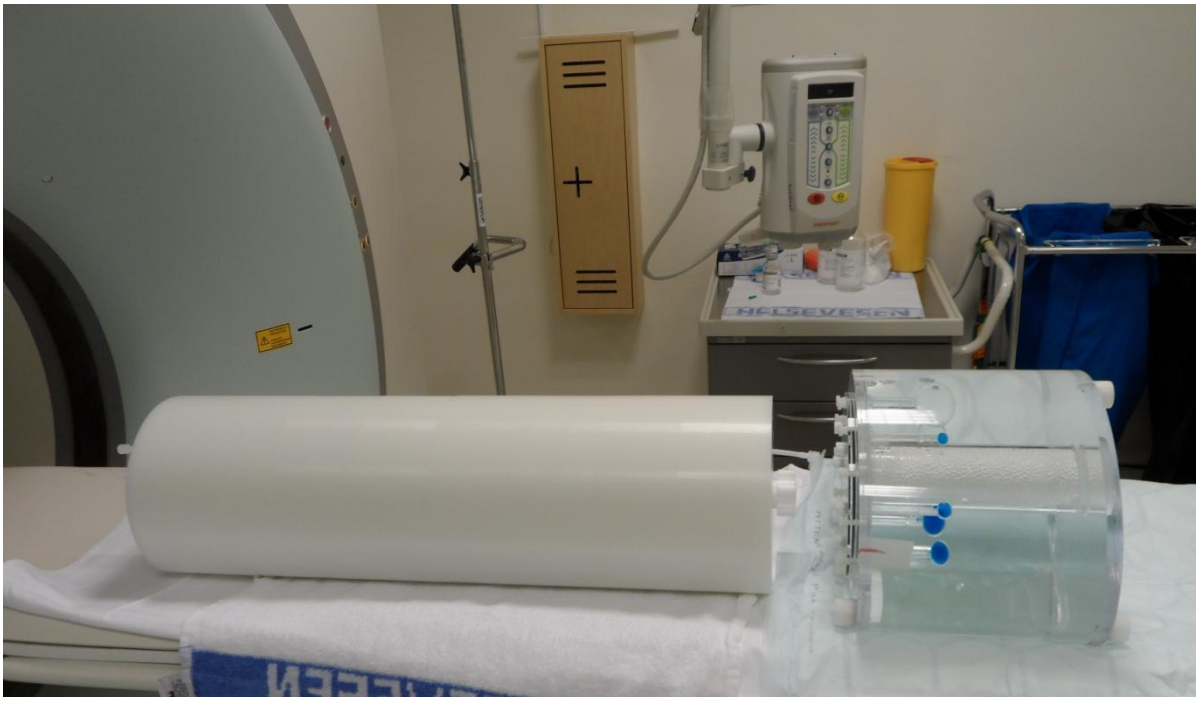

Figure 3.3: The prepared phantom on the bed of the PET/CT scanner ready for scanning. The blue coloured spheres are the spheres filled with F-18 activity.

3.2 Data collection and image reconstruction

For a standard clinical whole body PET/CT protocol studies, data were acquired using the following parameters (Table 3.1) [8]:

Transaxial slices through the axial centre of the spheres within the image phantom were reconstructed with a selection of reconstruction parameters and different image corrections applied to the data. These images reconstruction parameters are presented in table 3.1 below.

Table 3.1: Comparison between scanner parameters employed in this project work.

Standard clinical whole body PET/CT protocol	*Selected reconstruction parameters used*
Iterative reconstruction algorithm	Iterative reconstruction algorithm
Iterations: 4	Iterations: 4
Subsets: 8	Subsets: 8
Filter: Gaussian	Filters: Gaussian Median Hann Butterworth (Order: 1, 10 and 20)*
FWHM: 5 mm	FWHM: 5 (3, 4, 6, 7 and 8)** mm
Matrix size: 168 x 168 pixels	Matrix sizes: 128 x 128 pixels 168 x 168 pixels
Corrections: Attenuation and Scatter	Corrections: Attenuation and Scatter Only Attenuation

Tube current-time: 50 mAs (time = 5 sec) Time of PET scan: 3 minutes	No correction*** Tube current-time: 50 mAs (time = 5 sec) Time of PET scan: 3 minutes Slice thickness: 2.0 mm

* Butterworth filter: Used in combination with orders: 1, 10 and 20. The order is the strength of the filter.
** FWHM of 5 mm was used in combination with the various filters. Also, a Gaussian filter with FWHMs of 3, 4, 6, 7 and 8 mm was used and compared with the standard FWHM of 5 mm.
*** Only attenuation and no corrections were used in the case of the Gaussian filter only.

A selection of different reconstruction parameters was made to compare image qualities using the standard reconstruction parameters and other standard parameters in the same system as shown in the table above.

This was also done to assess the impact of applying different imaging reconstruction algorithms or technique to the image data. Henceforth, only selected parameters from the lot were applied on the acquired data for reconstruction.

The selected reconstruction parameters utilized were iterative reconstruction algorithm with iterations of 4 and subset of 8, Gaussian filter (with FWHMs of 3, 4, 5, 6, 7 and 8mm), Hann filter, Median filter and Butterworth filters (all with FWHM of 5 mm), and attenuation correction (of the CT bed scan) and scatter correction. Only attenuation correction and no corrections were used in the case of the Gaussian filter in order to compare with images that were corrected with both corrections. A matrix size of 168 x 168 pixels was also used and compared with a 128 x 128 pixel matrix size. For example, when a median filter is selected, the other parameters (iterative reconstruction, iterations: 4, subset: 8 FWHM: 5mm, matrix size: 128 x 128 pixels, attenuation and scatter corrections) were unaltered.

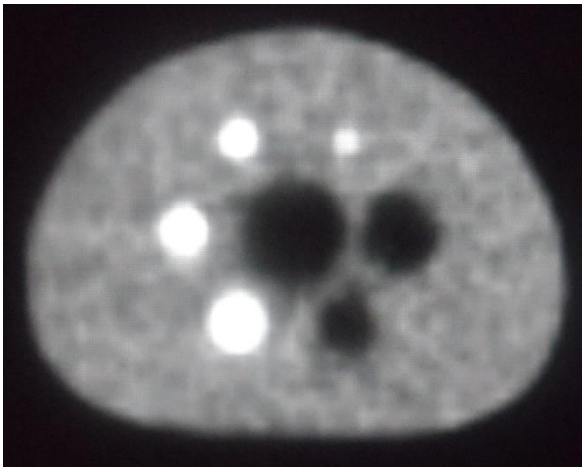

Figure 3.4: An image slice reconstructed with a Gaussian filter, FWHM of 5 mm, iterations of 4, subset of 8 and attenuation and scatter corrected.

3.3 Data processing

All slices were reconstructed and corrections applied. A centre slice where the image contrast was assumed to be high was selected from the image slices. Four other slices, two in both directions (to the selected centre slice) within a 1 cm and 2 cm distances were also selected making the total number of slices to be analyzed five.

Regions of interest (ROI) were drawn on each hot and cold sphere in the resulting images after reconstruction (figure 3.5: 'A'). Circular ROI were used with a diameter equal to the inner diameter of the spheres. Then ROIs of the same sizes were drawn in the background of the phantom on the centre slice. Twelve 37 mm diameter ROIs were drawn throughout the background (figure 3.5: 'B') such that it is at a distance of 15 mm from the edge of the phantom and no closer than 15 mm to any of the other spheres (figure 3.5). ROIs of the smaller spheres (28, 22, 17, 13, and 10 mm) were drawn (figure 3.5: 'C' and 'D') concentric to the 37 mm ROI drawn on the background. The same procedure for drawing of spheres was performed on the other four slices selected on both sides of the centre slice. Therefore, a total of sixty (60) ROIs of each sphere were drawn on the background.

A circular ROI, 30 mm in diameter were also drawn on the lung insert. Twelve other ROIs of the lung insert were drawn on the background, concentric to the 37 mm diameter ROI drawn. This was also done all five slices.

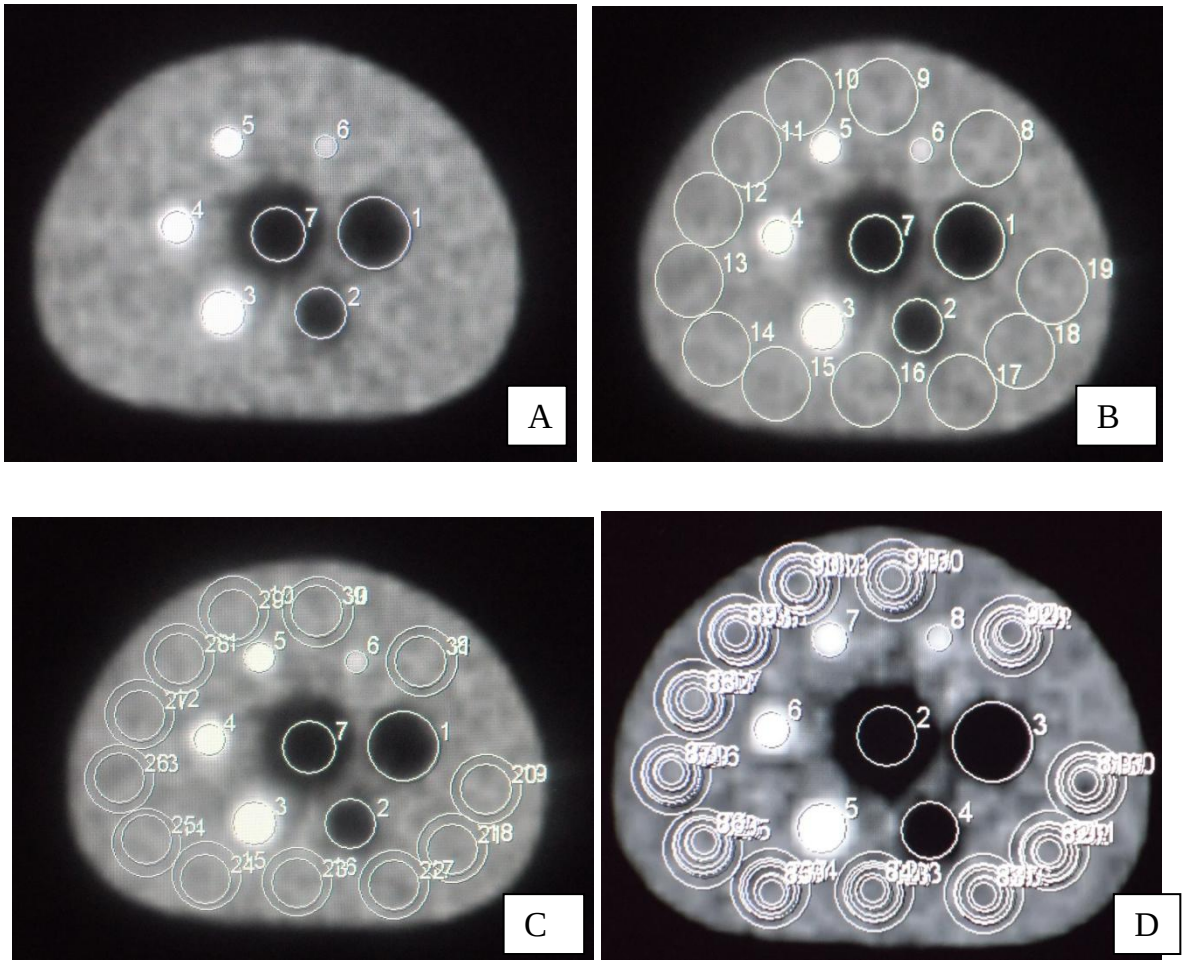

Figure 3.5: A)ROIs on only hot and cold spheres and lun insert B) ROIs of the 37 mm sphere C) and D) ROIs of the other spheres (28, 22, 17, 13, and 10 mm) and lung insert concentric to the 37 mmsphere for image quality analysis.

The average counts in each image slice ROI were recorded and utilized to perform calculations and evaluations of i) the percentage of recovery coefficient, ii) percentage background variability, iii) percentage relative error and iv) standard deviation on the quality of the reconstructed images. These image quality parameters mentioned were calculated based on the formulae stated in Chapter 3.4 below.

3.4 Formulae used for the data analysis

Image qualities for both hot and cold spheres were calculated as percentage contrast recovery coefficients apply equations {3.1} and {3.2} respectively. This was done to evaluate the contrast of both hot and cold spheres in a warm background:

a. $Q_{H,j}$ - percentage hot contrast recovery coefficient for sphere *j*, where *j* represents the 10, 13, 17 and 22 mm spheres.

b. $Q_{C,i}$ - percentage cold contrast recovery coefficient for sphere *i*, where *i* represents the 28 and 37 mm spheres.

$$Q_{H,j} = \frac{\frac{C_{H,j}}{C_{B,j}} - 1}{\frac{a_H}{a_B} - 1} \times 100\% \quad \{3.1\}$$

Where:

a. $C_{H,j}$ – the average counts in the ROI for sphere *j*

b. $C_{B,j}$ – the average of the background ROI counts for sphere *j*

c. a_H – the activity concentration in the hot spheres

d. a_B – the activity concentration in the background

$$Q_{C,i} = \left(1 - \frac{C_{C,i}}{C_{B,i}}\right) \times 100\% \quad \{3.2\}$$

Where:

a. $C_{C,i}$ – the average counts in the ROI for sphere *j*

b. $C_{B,i}$ – the average of the 60 background ROI counts for sphere *j*

The background variability (also called coefficient of variation) was calculated as part of the image quality measurement to evaluate how the mean counts of each sphere in the background vary from their corresponding mean counts in the original spheres with either activity or no activity.

N_x - coefficient of variation for all ROIs of size *x* (10, 13, 17, 22, 28 and 37 mm) in the image volume

Percentage background variability N_x for sphere *x* is given by:

$$N_x = \frac{SD_x}{C_{B,x}} \times 100\% \qquad \{3.3\}$$

Where SD_x is the standard deviation of the background ROI counts for sphere *x*, and is calculated as:

$$SD_x = \sqrt{\frac{\sum_{K=1}^{K} \left(C_{B,x,K} - C_{B,x} \right)^2}{K-1}} \quad ; \quad K = 60 \qquad \{3.4\}$$

$C_{B,x}$ – the average of the 60 background ROI counts for sphere *j*

Relative Count Error (ΔC) – The relative error (equation {3.5}) [5], was calculated to measure the difference between the expected counts and the measured counts in the images, expressed as a percentage. It is also calculated to measure the accuracy of attenuation and scatter corrections.

a. ΔC_{lung} – relative error in the lung insert

Relative error $\Delta C_{lung,i}$ expressed as percentage for each slice *i*:

$$\Delta C_{lung,i} = \frac{C_{lung,i}}{C_{B,i}} \times 100\% \qquad \{3.5\}$$

Where:

a. $C_{lung,i}$ – the average counts in the lung insert ROI

b. $C_{B,i}$ – the average of the 60 background ROI of the lung insert.

3.5 Analysis with an automatic Python program

The description of how the data sets were processed and analyzed above in section 3.5 was done manually on the Siemens Biograph PET/CT workstation. However [31], developed a an automatic python program that could do exactly the data processing and calculation automatically by reading the image files which were in digital image and communications in medicine (DICOM) format.

Given a threshold value, the program finds values (counts) in the DICOM files that are higher than the threshold value and labels them as white in the image pixel. Depending on

how big the value is from the threshold value, the pixel in that position of the image becomes whiter. All values less than the threshold value are set to black in the image. The pixels were then connected in the x-y-z plane due to their positions in the image. The pixels that are connected forms a cluster. Based on the size of the cluster, the size of a sphere is computed. The program then finds the edge of the phantom and calculates 15 mm from the edge and places the 37 mm sphere at that position. This was done to find regions where 12 ROI of the 37 mm can be placed in the image (figure 3.6).

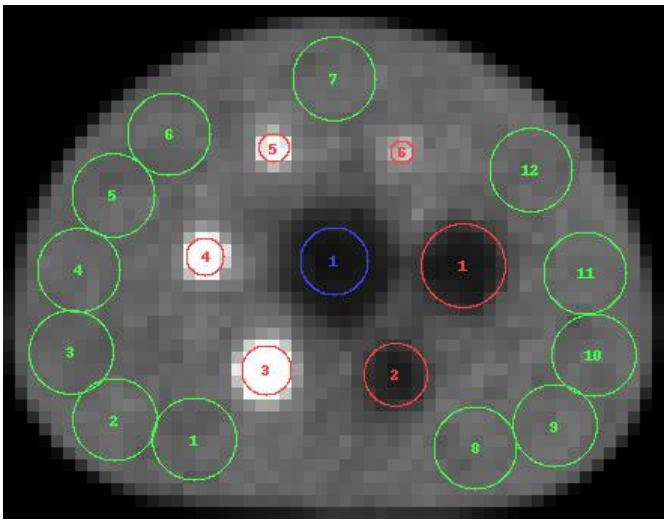

Figure 3.6: An image with ROIs from the automatic python program. The image was reconstructed with the standard clinical whole-body PET/CT but with a matrix size of 128 x 128 pixels.

4. RESULTS

The different compartments of the NEMA IEC Body Phantom was prepared as described in Chapters 3.1.1 to 3.1.4 and scanned with the standard clinical whole body PET/CT protocol (Chapters 3.1.5 and 3.2) on a Siemens Biograph scanner [7]. Experiments were conducted with both a sphere-to-background ratio (SBR) of 4:1 and 8:1. Three repetitive studies were done for each concentration ratio. Transaxial slices through the axial centre of the spheres within the image quality phantom were reconstructed using a selection of reconstruction parameters and different image corrections. Percent contrast recovery and percent background variability were computed for each sphere together with the residual error in the lung insert caused by attenuation and scatter corrections, as described in Chapters 2.8.1 and 2.8.2. Chapters 3.3 and 3.4 describe the data processing procedure and the equations used for the computations. The image quality results are presented in Chapters 4.1 – 4.3 below.

4.1 Image quality results following the NEMA NU 2-2007 protocol

Image quality results in images reconstructed with a standard whole body PET/CT protocol (Chapter 3.2) and a SBR of 4:1 and 8:1 are given in Chapter 4.1.1 and 4.1.2 respectively. For each concentration ratio the results from the third experiment are listed, followed by the mean values and standard deviations from the three repetitive experiments.

The mean SBR from the three experiments of each concentration ratio, were 4.2 ± 0.1 (for SBR of 4:1) and 8.5 ± 0.2 (for SBR of 8:1). These measured SBR values deviated from the recommended SBRs of 4:1 and 8:1 by 5 % and 6 % respectively.

4.1.1 Sphere-to-background activity ratio of 4:1

The data analyses results obtained by the use of equations {3.1} to {3.5} on images reconstructed from the third experiment with a SBR of 4:1 are given in table 4.1. Table 4.2 show the mean values and the standard deviations from all three experiments performed with 4:1 SBR. From tables 4.1 and 4.2 it is obvious that the contrast recovery coefficients for both hot and cold spheres increases with increasing sphere diameter (10 – 37 mm). The mean hot contrast recovery coefficient increases from 13.7 % for the 10 mm sphere to 42.6 % for the 22 mm sphere, while the mean cold contrast recovery coefficient has a smaller increase from

57.8 % for the 28 mm sphere to 60.1 % for the 37 mm sphere. The mean background variability shows the opposite trend, it is decreasing from 6.8 % for the 10 mm sphere to 2.6 % for the 37 mm sphere. The accuracy of attenuation and scatter correction is, as described in section 3.4 in Chapter 3, given by the lung insert relative error. For SBR of 4:1, the mean relative error for all three experiments is 22.0 % (Table 4.2).

The standard deviations in contrast recovery and background variability in table 4.2 show fluctuations between the measured values obtained in the three repetitive experiments. The standard deviations related to contrast recovery coefficient varies in Table 4.2 from 0.6 % (37 mm sphere) to 4.3 % (17 mm sphere). The standard deviations in the background variability is less than or equal to 0.6 %.

Table 4.1: NEMA Image quality results for 4:1 sphere-to-background ratio and standard whole body PET/CT acquisition and reconstruction protocol. The 28 and 37 mm spheres are filled with non-radioactive water (cold contrast) while the remaining spheres are filled with a solution of F18 (hot contrast).

Sphere diameters	Contrast recovery coefficient (%)	Background variability (%)
10 mm	15.2	6.5
13 mm	16.5	5.8
17 mm	26.2	3.8
22 mm	40.1	3.5
28 mm	57.7	3.1
37 mm	59.3	2.4
Lung insert (relative error)		21.9 %

Table 4.2: Mean values and standard deviation of three repetitive NEMA Image quality experiment for 4:1 sphere-to-background ratio and standard whole body PET/CT acquisition and reconstruction protocol. The 28 and 37 mm spheres are filled with non-radioactive water (cold contrast) while the remaining spheres are filled with a solution of F18 (hot contrast).

Sphere diameters	Mean Contrast recovery	Mean Background variability (%)
10 mm	13.7 ± 1.8	6.8 ± 0.6
13 mm	20.2 ± 3.2	5.9 ± 0.4
17 mm	30.7 ± 4.3	4.0 ± 0.2
22 mm	42.6 ± 2.8	3.6 ± 0.3
28 mm	57.8 ± 1.3	3.1 ± 0.3
37 mm	60.1 ± 0.6	2.6 ± 0.5
Lung insert (mean relative error)		(22.0 ± 0.1) %

4.1.2 Sphere-to-background activity ratio of 8:1

The data analyses results from the third experiment with a SBR of 8:1 are given in table 4.3. Table 4.4 shows the mean values and the standard deviations from all three experiments with 8:1 SBR.

As for the 4:1 SBR, table 4.3 and 4.4 shows that the contrast recovery coefficient for the 8:1 SBR increases with increasing sphere diameter while the background variability decreases with increasing sphere diameter. From table 4.4, the mean hot contrast recovery coefficient increases from 16.3 % for the 10 mm sphere to 41.9 % for the 22 mm sphere. When comparing the mean contrast recovery coefficients for SBR of 4:1 to the results for 8:1 SBR (Table 4.2 and Table 4.4), it seems as the contrast recovery for the smaller spheres (10 – 17 mm) is somewhat higher for the 8:1 SBR compared to the 4:1 SBR. For the largest hot contrast sphere (22 mm) and the two cold contrast spheres (28 and 37 mm), the contrast recovery is slightly lower for a SBR of 8:1 compared to SBR of 4:1. The mean cold contrast recovery coefficient for the 37 mm sphere is slightly higher with 55.0 %, compared to the 28 mm sphere with 51.6 %. The mean background variability for the SBR of 8:1 decreases from 6.5 % for the 10 mm sphere to 2.7 % for the 37 mm sphere (Table 4.4). These results are in the same range as the mean background variability for the SBR of 4:1 (Table 4.2).

The relative error related to the accuracy of attenuation and scatter correction is fairly larger with 24.0 %, for SBR of 8:1 (Table 4.4) compared to the error of 22.0 % measured for SBR of 4:1.

Table 4.3: NEMA Image quality results for 8:1 sphere-to-background ratio and standard whole body PET/CT acquisition and reconstruction protocol. The 28 and 37 mm spheres are filled with non-radioactive water (cold contrast) while the remaining spheres are filled with a solution of F18 (hot contrast).

Sphere diameters	Contrast recovery coefficient (%)	Background variability (%)
10 mm	17.9	6.7
13 mm	21.9	5.9
17 mm	34.2	5.5
22 mm	39.7	4.5
28 mm	46.9	3.8
37 mm	52.6	3.0
Lung insert relative error		24.9 %

Table 4.4: Mean values and standard deviation of three repetitive NEMA Image quality experiments for 8:1 sphere-to-background ratio and standard whole body PET/CT acquisition and reconstruction protocol. The 28 and 37 mm spheres are filled with non-radioactive water (cold contrast) while the remaining spheres are filled with a solution of F18 (hot contrast).

Sphere diameters	Mean Contrast recovery coefficient (%)	Mean Background variability (%)
10 mm	16.3 ± 6.8	6.5 ± 0.3
13 mm	22.8 ± 2.5	5.3 ± 0.5
17 mm	34.7 ± 3.2	4.6 ± 1.1
22 mm	41.9 ± 3.6	3.9 ± 0.3
28 mm	51.6 ± 2.7	3.4 ± 0.3
37 mm	55.0 ± 2.5	2.7 ± 0.2
Lung insert relative error		(24.0 ± 0.2) %

The standard deviations in contrast recovery coefficient and background variability Tables 4.4 show fluctuations between the measured values obtained in repetitive experiments. For 8:1 SBR the contrast recovery standard deviations are somewhat higher than for the 4:1 SBR, varying from 2.5 % (13 and 37 mm sphere) to 6.8 % (10 mm sphere). The standard deviation in the background variability is less than or equal to 1.1 % for SBR of 8:1.

4.2 Image quality result using different reconstruction parameters

In order to investigate how different reconstruction parameters, such as image filters, filter width and matrix size, influence PET image quality, the acquired data sets from section 4.1 were reconstructed with a selection of these parameters. Image quality results in images reconstructed with Gaussian filters with different full width at half maximum (FWHM) are given in Chapter 4.2.1, image quality results for different types of image filters are given in Chapter 4.2.2, image quality results for different corrections applied are given in section 4.2.3 and image quality results for different matrix sizes are given in Chapter 4.2.4.

4.2.1 Contrast recovery in images with different Gaussian filter width (FWHM)

The acquired data sets for the 4:1 and 8:1 SBRs were all reconstructed with Gaussian filter FWHMs of 3, 5 and 7 mm respectively, keeping the other reconstruction parameters constant (iterative reconstruction with 4 iterations and 8 subsets, matrix size of 128 and zoom of 1). The image quality results are given in total in tables B.1 to B.4 in Appendix B.

Figure 4.1 shows the contrast recovery coefficient result for the third 4:1 concentration ratio experiment with FWHM of 3, 5 and 7 mm. Figure 4.2 shows the mean contrast recovery

coefficient with standard deviation (error bars) for the three repetitive experiments. Tables B. 1 and B.2 in Appendix B shows the total image quality results with a SBR of 4:1 and different Gaussian FWHMs.

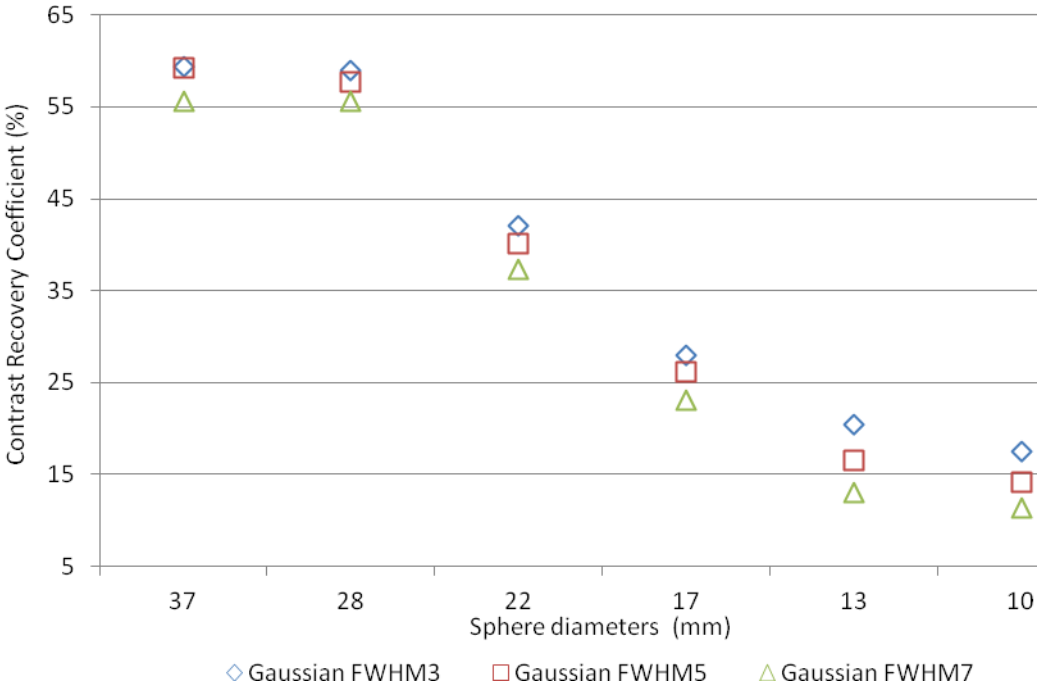

Figure 4.1: Contrast recovery coefficient values in images of the NEMA phantom with a sphere-to-background ratio of 4:1. The images are reconstructed using Gaussian filters with FWHM of 3, 5 and 7 mm. The 28 and 37 mm spheres are filled with non-radioactive water (cold contrast) while the remaining spheres are filled with a solution of F18 (hot contrast).

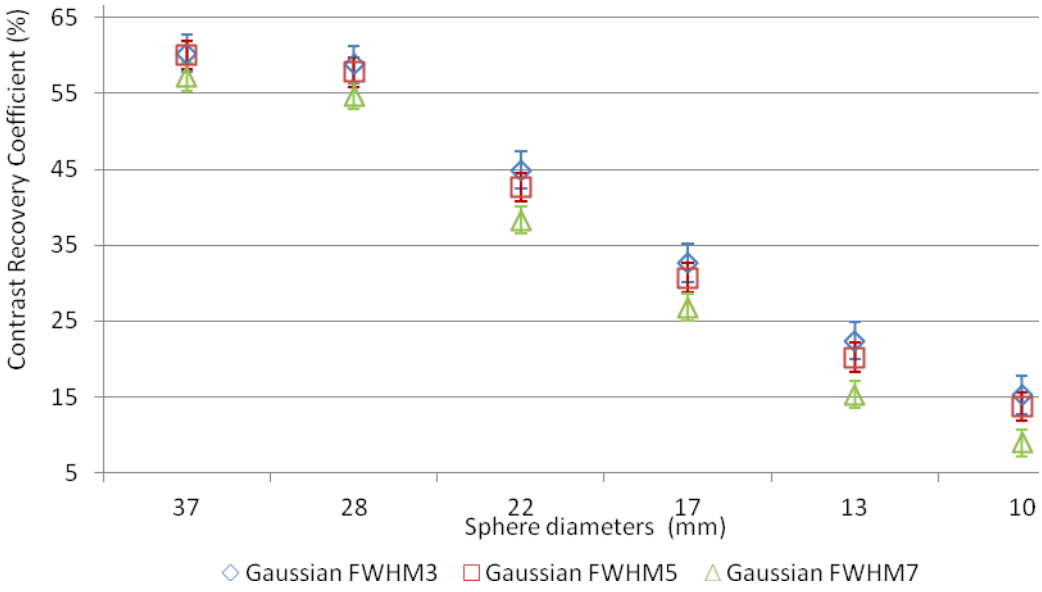

Figure 4.2: Mean contrast recovery coefficient values with standard deviation (error bars) of three repetitive NEMA image quality experiments for 4:1 sphere-to-background ratio. The images are reconstructed using Gaussian filters with FWHM of 3, 5 and 7 mm. The 28 and 37 mm spheres are filled with non-radioactive water (cold contrast) while the remaining spheres are filled with a solution of F18 (hot contrast).

Similar analysis with SBR of 8:1 are shown in figures 4.3 and 4.4. Table B.3 and B.4 in appendix B shows the image quality result for SBR 8:1 in its entirety.

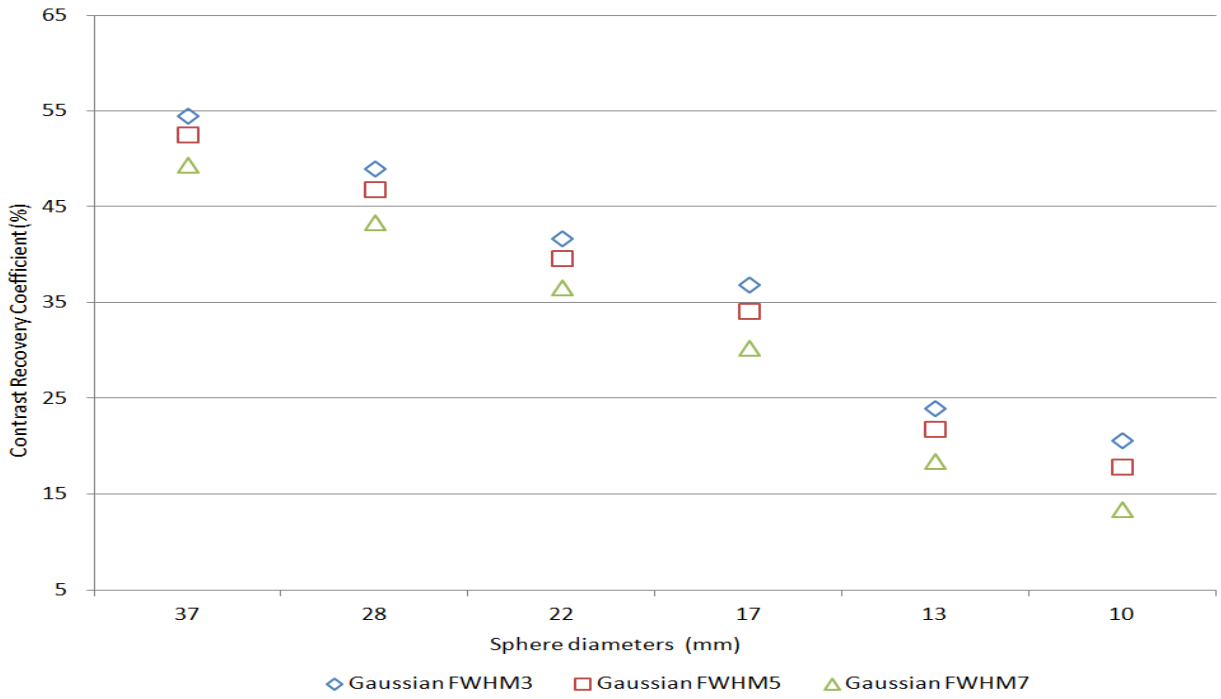

Figure 4.3: Contrast recovery coefficient values in images of the NEMA phantom with a sphere-to-background ratio of 8:1. The images are reconstructed using Gaussian filters with FWHM of 3, 5 and 7 mm. The 28 and 37 mm spheres are filled with non-radioactive water (cold contrast) while the remaining spheres are filled with a solution of F18 (hot contrast).

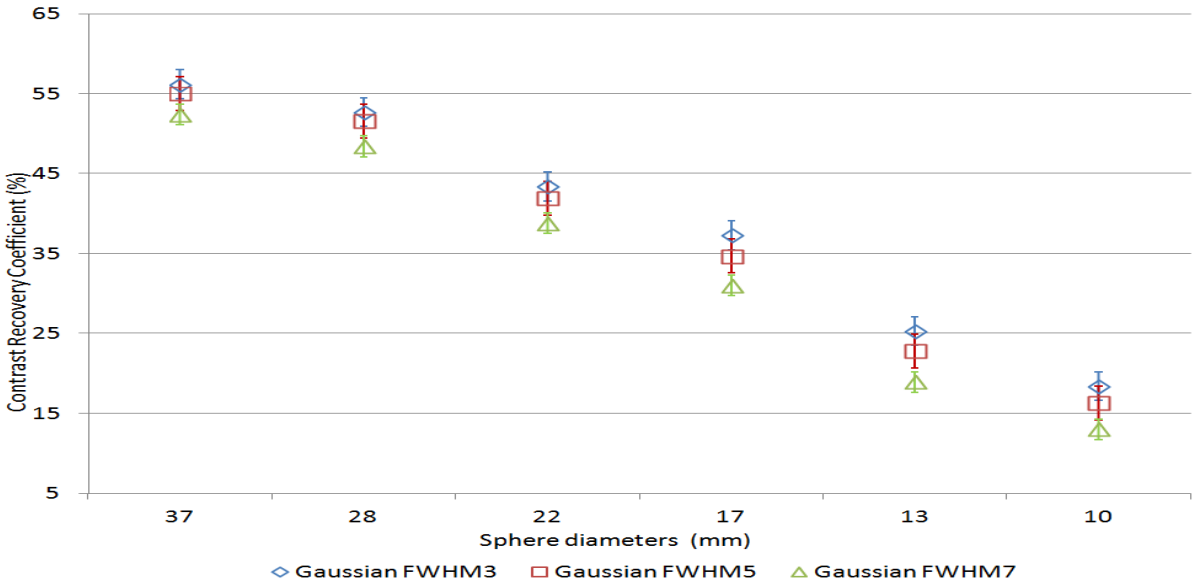

Figure 4.4: Mean contrast recovery coefficient values with standard deviation (error bars) of three repetitive NEMA image quality experiments' for 8:1 sphere-to-background radio. The images are reconstructed using Gaussian filters with FWHM of 3, 5 and 7 mm. The 28 and 37 mm spheres are filled with non-radioactive water (cold contrast) while the remaining spheres are filled with a solution of F18 (hot contrast).

Figure 4.1 and 4.2 (SBR 4:1) shows that the overall contrast recovery increases as FWHM decreases. This effect seems to become more prominent for smaller hot spheres than for larger spheres. For the 10 mm sphere the mean contrast recovery increases with 71 %, from 8.9 % to 15.2 %, when the FWHM decreases from 7 mm to 3 mm (Table B.2, Appendix B). While for the 22 mm sphere, the mean contrast recovery increases with 17 %, from 38.3 to 44.9 %, when the FWHM decreases from 7 to 3 mm (Table B.2, Appendix B). For the cold spheres (28 and 37 mm) there seem to be only a small difference between the contrast recovery coefficients with varying FWHMs.

The contrast recovery results for SBR of 8:1 in figures 4.3 - 4.4 and Tables B.3 – B.4, show similar trends as described for SBR 4:1 with varying FWHM values. The contrast recovery increases for all sphere sizes with decreasing FWHM values. As for SBR of 4:1, there is an improvement in contrast recovery when FWHM is decreasing which seems to be more prominent for the smaller hot spheres (42 % higher recovery for the 10 mm sphere when FWHM decreases from 7 to 3 mm, Table B.4) than for the larger hot spheres (14 % improvement for the 22 mm sphere when FWHM decreases from 7 to 3 mm, Table B.4). The cold contrast recovery seems to be less influenced by different FWHM as for the 4:1 SBR.

Comparing the results in Table B.4 and Table B.2 it seems that the contrast recovery is higher in the 10 to 17 mm hot spheres with 8:1 SBR for all FWHMs, compared to the results for 4:1 SBR. For the biggest hot sphere (22 mm) and the two cold spheres (28 and 37 mm) the contrast recovery is either close to equal or higher in the 4:1 SBR compared to the 8:1 SBR. But taking into account the range of these measurements, it is apparent that most of the differences between 4:1 and 8:1 SBR are less than the corresponding standard deviations.

4.2.2 Image quality result using different reconstruction filters

The acquired data sets were also reconstructed with a selection of different image reconstruction filters available on the Siemens Biograph PET/CT scanner; see section 3.2 in Chapter 3. The remaining reconstruction parameters (iterative reconstruction with 4 iterations and 8 subsets, matrix size of 128, scatter and attenuation corrections) were unaltered.

Image quality results from the analyses on images reconstructed from the third data set (SBR 4:1) with a FWHM of 5 mm and respectively a Gaussian filter, a median filter, a Hann filter and a Butterworth filter with an order of 10 (O10), are given in table 4.5. Table 4.6 gives the mean values and the standard deviations from all three experiments for SBR of 4:1 with the same selection of image filters and FWHM. Corresponding image quality results from analyses of the data sets acquired with a SBR of 8:1 are given in tables 4.7 and 4.8.

Table 4.5: NEMA Image quality results for 4:1 sphere-to-background ratio and different image filters with FWHM of 5 mm. The 28 and 37 mm spheres are filled with non-radioactive water (cold contrast) while the remaining spheres are filled with a solution of F-18 (hot contrast).

Sphere diameters	Contrast recovery coefficient, % (Background variability, %)			
	Gaussian filter	Median filter	Hann filter	Butterworth filter O10
10 mm	15.2 (6.5)	11.3 (7.2)	15.8 (9.1)	18.5 (11.6)
13 mm	16.5 (5.8)	12.1 (5.8)	16.9 (7.7)	22.4 (10.2)
17 mm	26.2 (3.8)	23.8 (3.6)	26.5 (4.3)	29.0 (5.7)
22 mm	40.1 (3.5)	36.9 (3.4)	40.2 (4.1)	42.0 (5.3)
28 mm	57.7 (3.1)	60.1 (2.6)	60.0 (3.0)	62.2 (3.9)
37 mm	59.3 (2.4)	57.0 (1.8)	57.8 (1.7)	58.6 (2.0)
Lung insert (relative error)	21.9 %	22.9 %	22.5 %	21.9 %

Table 4.6: Mean values and standard deviation of three repetitive NEMA Image quality experiments for 4:1 sphere-to-background ratio and different image filters with FWHM of 5 mm. The 28 and 37 mm spheres are filled with non-radioactive water (cold contrast) while the remaining spheres are filled with a solution of F-18 (hot contrast).

Sphere diameters	Mean Contrast recovery coefficient, % (Mean Background variability, %)			
	Gaussian filter	Median filter	Hann filter	Butterworth filter O10
10 mm	13.7 ± 1.8 (6.8 ± 0.6)	9.3 ± 2.0 (6.8 ± 0.5)	13.2 ± 1.7 (8.3 ± 0.6)	17.1 ± 1.8 (10.2 ± 1.2)
13 mm	20.2 ± 3.2 (5.9 ± 0.4)	14.6 ± 2.5 (5.6 ± 0.2)	18.9 ± 3.0 (6.1 ± 0.8)	24.8 ± 2.3 (8.9 ± 1.4)
17 mm	30.7 ± 4.3 (4.0 ± 0.2)	28.0 ± 3.8 (4.0 ± 0.5)	30.1 ± 3.8 (4.3 ± 0.0)	33.1 ± 3.9 (5.8 ± 0.1)
22 mm	42.6 ± 2.8 (3.6 ± 0.3)	39.3 ± 2.5 (3.7 ± 0.5)	42.2 ± 2.6 (4.1 ± 0.1)	45.3 ± 2.3 (5.3 ± 0.0)
28 mm	57.8 ± 1.3 (3.1 ± 0.3)	59.1 ± 1.3 (3.1 ± 0.8)	59.2 ± 1.3 (3.2 ± 0.4)	60.7 ± 1.1 (4.4 ± 0.5)
37 mm	60.1 ± 0.6 (2.6 ± 0.5)	58.8 ± 1.6 (2.3 ± 0.7)	59.5 ± 1.6 (2.1 ± 0.7)	59.9 ± 1.4 (3.2 ± 0.7)
Lung insert relative error	(22.0 ± 0.1) %	(22.7 ± 0.4) %	(22.3 ± 0.1) %	(21.8 ± 0.1) %

Table 4.7: NEMA Image quality results for 8:1 sphere-to-background ratio and different image filters with FWHM of 5 mm. The 28 and 37 mm spheres are filled with non-radioactive water (cold contrast) while the remaining spheres are filled with a solution of F-18 (hot contrast).

Sphere diameters	Contrast recovery coefficient, % (Background variability, %)			
	Gaussian filter	Median filter	Hann filter	Butterworth filter O10
10 mm	17.9 (6.7)	10.3 (6.1)	17.7 (6.8)	21.9 (5.8)
13 mm	21.9 (5.9)	13.7 (5.7)	22.5 (6.1)	25.8 (4.8)
17 mm	34.2 (5.5)	30.5 (5.2)	34.3 (5.8)	37.1 (3.3)
22 mm	39.7 (4.5)	37.2 (4.3)	40.0 (4.7)	42.2 (3.1)
28 mm	46.9 (3.8)	43.9 (3.8)	46.9 (3.9)	49.7 (2.8)
37 mm	52.6 (3.0)	53.7 (3.1)	52.8 (3.4)	54.5 (2.1)
Lung insert relative error	24.9 %	24.6 %	21.8 %	22.5 %

Table 4.8: Mean values and standard deviation of three repetitive NEMA Image quality experiments for 8:1 sphere-to-background ratio and different image filters with FWHM of 5 mm. The 28 and 37 mm spheres are filled with non-radioactive water (cold contrast) while the remaining spheres are filled with a solution of F-18 (hot contrast).

Sphere diameters	Mean Contrast recovery coefficient, % (Mean Background variability, %)			
	Gaussian filter	Median filter	Hann filter	Butterworth filter O10
10 mm	16.3 ± 6.8 (6.5 ± 0.3)	9.3 ± 2.0 (6.3 ± 0.1)	15.2 ± 5.5 (6.6 ± 0.5)	19.1 ± 7.8 (7.2 ± 1.2)
13 mm	22.8 ± 2.5 (5.3 ± 0.5)	15.5 ± 3.7 (5.3 ± 0.5)	21.1 ± 1.7 (5.8 ± 0.4)	26.9 ± 3.7 (6.0 ± 0.6)
17 mm	34.7 ± 3.2	30.7 ± 3.0	33.6 ± 5.9	37.8 ± 4.5

	(4.6 ± 1.1)	(4.6 ± 0.7)	(5.1 ± 1.0)	(4.7 ± 0.7)
22 mm	41.9 ± 3.6 (3.9 ± 0.3)	39.9 ± 2.8 (3.9 ± 0.3)	40.2 ± 1.9 (4.5 ± 1.2)	44.8 ± 2.0 (4.2 ± 0.5)
28 mm	51.6 ± 2.7 (3.4 ± 0.3)	49.9 ± 7.4 (3.5 ± 0.4)	51.3 ± 6.2 (3.5 ± 0.4)	56.6 ± 5.9 (3.6 ± 0.8)
37 mm	55.0 ± 2.5 (2.7 ± 0.2)	55.6 ± 2.9 (2.9 ± 0.2)	54.9 ± 2.3 (3.0 ± 0.5)	54.8 ± 0.3 (2.3 ± 0.6)
Lung insert relative error	(24.0 ± 0.2) %	(23.9 ± 0.2) %	(23.1 ± 0.3) %	(23.0 ± 0.3) %

The image quality results for both 4:1 and 8:1 SBR and the different image filters selected shows that the contrast recovery coefficient increases when the diameter of the sphere increases; whereas the background variability decreases as the sphere diameter increases. This is consistent with the obtained results in Chapters 4.1.1, 4.1.2 and 4.2.1.

From tables 4.5 - 4.8 it appears that the Butterworth filter (O10) results in higher contrast recovery coefficient compared to the other filters for all hot contrast spheres (10 – 22 mm) and for both the SBR of 4:1 and 8:1. For 8:1SBR in Table 4.8, the Butterworth filter's (O10) contrast recovery coefficient for the 10 mm sphere is respectively 26, 105 and 41 % higher than the Hann, Median and Gaussian filter respectively. For the 4:1 SBR in Table 4.6, the Butterworth filter's (O10) contrast recovery coefficient for the 10 mm sphere is respectively 30, 84 and 25 % higher than the Hann, Median and Gaussian filter. The images reconstructed with the Gaussian filter and the Hann filter have overall similar values for the hot contrast spheres (10 – 22 mm). The difference in contrast recovery coefficient between these two filters ranges from 0 to 4 %. The Median filter tends to give the lowest contrast recovery values in the majority of the analysis. As an example, the Median filter for the 13 mm sphere with 8:1 SBR in table 4.8 is gives respectively 47, 36 and 74 % lower contrast recovery values compared to the Gaussian, Hann and Butterworth filter (O10). For the cold contrast spheres (28 and 37 mm) there seems to be less differences in the measured recovery coefficient values and also a less recognizable pattern comparing the results obtained from the different image filters.

There seem not to be a specific pattern concerning the standard deviations for the contrast recovery values measured between the different filters for either SBR of 4:1 or 8:1. From table 4.6 (SBR of 4:1), the standard deviations related to the contrast recovery coefficient varies between 0.6 and 4.3 % for the Gaussian filter, 1.3 and 3.8 % for the Median filter, 1.3

and 3.8 % for the Hann filter, and 1.1 and 3.9 % for the Butterworth filter (O10). In table 4.8 (SBR of 8:1), the variations are between 2.5 and 6.8 % for the Gaussian filter, 2.0 and 7.4 % for the Median filter, 2.5 and 1.7 % for the Hann filter, and 0.3 and 7.8 % for the Butterworth filter (O10).

The relative error due to attenuation and scatter corrections gives values in the same range for all image filters used for both SBRs. The relative errors measured in the Gaussian filter, Median filter, Hann filter, and Butterworth filter (O10), ranges respectively from 21.8 to 22.7 % for the SBR of 4:1 and 23.0 to 24.0 % for SBR of 8:1(Tables 4.6 and 4.8).

The background variability measured appears to be much higher in images reconstructed with the Butterworth filter (O10) compared to the other filters for the 4:1 SBR (Table 4.6). For the 8:1 SBR (Table 4.8), there is less recognise pattern between the different filters' background variability values measured. The standard deviations in the background variability are less than or equal to 0.9 % for all the reconstruction filters employed with SBR of 4:1 and less than or equal to 2.1 % for all the reconstruction filters employed with SBR of 8:1.

4.2.3 Image quality results when different image corrections were applied

Different mathematical corrections can be applied in reconstruction of PET images as described in Chapters 3.0, 3.2 and 3.4. Corrections available during image reconstruction on the Siemens Biograph PET/CT scanner are attenuation correction together with scatter correction or attenuation correction only.

Image quality results from the analyzes on reconstructed images of the third data set (SBR 4:1) with attenuation and scatter corrections, no correction and only attenuation corrections applied are given in table 4.9. The remaining reconstruction parameters were unaltered (iterative reconstruction with 4 iterations and 8 subsets, Gaussian filter with FWHM of 5 mm and matrix size of 128). Table 4.10 gives the mean values and the standard deviations from all three experiments for SBR of 4:1 with the same selection of corrections applied. Results from analysis for the data sets acquired corresponding to a SBR of 8:1, are given in tables 4.11- 4.12.

Table 4.9: NEMA Image quality results for 4:1 sphere-to-background ratio when different corrections were applied. The 28 and 37 mm spheres are filled with non-radioactive water (cold contrast) while the remaining spheres are filled with a solution of F-18 (hot contrast).

Sphere diameters	Contrast recovery coefficient (%)			Background variability (%)		
	Attenuation and Scatter	Only Attenuation	No Correction	Attenuation and Scatter	Only Attenuation	No Correction
10 mm	14.2	14.0	2.2	6.5	9.4	23.0
13 mm	16.5	16.0	4.4	5.8	8.4	21.8
17 mm	26.2	25.8	7.2	3.8	5.7	23.0
22 mm	40.1	36.4	14.6	3.5	5.7	24.4
28 mm	57.7	26.9	82.0	3.1	4.8	24.0
37 mm	59.3	36.2	75.0	2.4	5.0	28.2
Lung inserts relative error				21.9 %	32.3 %	49.8 %

Table 4.10: Mean values and standard deviation of three repetitive NEMA Image quality experiments for 4:1 sphere-to-background ratio when different corrections were applied. The 28 and 37 mm spheres are filled with non-radioactive water (cold contrast) while the remaining spheres are filled with a solution of F-18 (hot contrast).

Sphere diameters	Mean Contrast recovery coefficient (%)			Mean Background variability (%)		
	Attenuation and Scatter	Only Attenuation	No Correction	Attenuation and Scatter	Only Attenuation	No Correction
10 mm	13.7 ± 1.8	12.2 ± 2.4	2.0 ± 1.0	6.8 ± 0.6	9.4 ± 2.2	23.0 ± 2.7
13 mm	20.2 ± 3.2	18.3 ± 2.4	3.8 ± 1.3	5.9 ± 0.4	8.4 ± 2.2	21.8 ± 2.4
17 mm	30.7 ± 4.3	28.8 ± 4.3	7.9 ± 1.2	4.0 ± 0.2	5.7 ± 0.4	23.0 ± 2.7
22 mm	42.6 ± 2.8	36.8 ± 1.4	16.3 ± 1.9	3.6 ± 0.3	5.7 ± 0.2	24.4 ± 0.8
28 mm	57.8 ± 1.3	25.3 ± 2.0	81.6 ± 1.2	3.1 ± 0.3	4.8 ± 0.1	24.0 ± 2.3
37 mm	60.1 ± 0.6	34.6 ± 2.2	78.4 ± 2.1	2.6 ± 0.5	5.0 ± 0.3	28.2 ± 4.9
Lung inserts relative error				(22.0 ± 0.1) %	(31.4 ± 0.8) %	(51.7 ± 2.7) %

Table 4.11 NEMA Image quality results for 8:1 sphere-to-background ratio when different corrections were applied. The 28 and 37 mm spheres are filled with non-radioactive water (cold contrast) while the remaining spheres are filled with a solution of F-18 (hot contrast).

Sphere diameters	Contrast recovery coefficient (%)			Background variability (%)		
	Attenuation and Scatter	Only Attenuation	No Correction	Attenuation and Scatter	Only Attenuation	No Correction
10 mm	17.9	14.7	8.5	6.7	6.3	19.8
13 mm	21.9	18.0	11.7	5.9	6.7	20.2
17 mm	34.2	28.9	18.1	5.5	6.3	22.2
22 mm	39.7	33.7	21.8	4.5	5.4	18.9
28 mm	46.9	17.8	80.9	3.8	4.9	17.3
37 mm	52.6	26.9	81.3	3.0	5.1	20.1
Lung inserts relative error				24.9 %	26.5 %	46.8 %

Table 4.12: Mean values and standard deviation of three repetitive NEMA Image quality experiments for 8:1 sphere-to-background ratio when different corrections were applied. The 28 and 37 mm spheres are filled with non-radioactive water (cold contrast) while the remaining spheres are filled with a solution of F-18 (hot contrast).

Sphere diameters	Mean Contrast recovery coefficient (%)			Mean Background variability (%)		
	Attenuation and Scatter	Only Attenuation	No Correction	Attenuation and Scatter	Only Attenuation	No Correction
10 mm	16.3 ± 6.8	13.5 ± 5.8	8.0 ± 5.9	6.5 ± 0.3	6.4 ± 0.2	17.2 ± 4.1
13 mm	22.8 ± 2.5	18.1 ± 1.0	12.8 ± 2.8	5.3 ± 0.5	8.6 ± 3.6	17.1 ± 5.5
17 mm	34.7 ± 3.2	28.8 ± 2.4	18.9 ± 1.5	4.6 ± 1.1	5.8 ± 0.5	17.9 ± 4.8
22 mm	41.9 ± 3.6	35.2 ± 1.5	24.2 ± 2.8	3.9 ± 0.3	5.4 ± 1.2	16.5 ± 5.2
28 mm	51.6 ± 2.7	21.5 ± 3.3	80.1 ± 1.6	3.4 ± 0.3	4.8 ± 1.3	16.1 ± 5.8
37 mm	55.0 ± 2.5	28.7 ± 8.1	79.1 ± 2.0	2.7 ± 0.2	5.9 ± 0.9	19.4 ± 3.2
Lung inserts relative error				(24.0 ± 0.2) %	(30.4 ± 3.4) %	(51.3 ± 4.6) %

From tables 4.9 - 4.12 it appears that images corrected with both attenuation and scatter gives higher hot contrast recovery coefficient than only attenuated and non corrected images. In table 4.10 (SBR of 4:1), the hot contrast recovery coefficient for images corrected with both attenuation and scatter are averagely 11 and 366 % higher than images corrected with only attenuation and non corrected images respectively. For the cold spheres, images corrected with both attenuation and scatters are averagely 101 % higher than only attenuation corrected images but 36 % less than non corrected images. Likewise in table 4.12 (SBR of 8:1), the hot contrast recovery coefficient for images corrected with both attenuation and scatter are averagely 22 and 85 % (for the hot spheres) higher than only attenuation corrected images and non corrected images respectively. In the cold spheres, images corrected with both attenuation and scatters are averagely 116 % higher than only attenuation corrected images. However, they are 40 % less than non corrected images.

The mean background variability is largest (Table 4.10) in images with no correction, which for the hot spheres are in an average of 390 and 234 % higher than in images corrected with both attenuation and scatter and only attenuation corrected images respectively (SBR of 4:1). For the cold spheres non corrected images' mean background variability is averagely 829 and 432 % higher than images corrected for both attenuation and scatter and only attenuation corrected images respectively. In table 4.12 (SBR of 8:1), the mean background variability for images with no correction is higher (for the spheres 10 – 37 mm) than images corrected

for both attenuation and scatter and only attenuation corrected images by an average of 284 and 191 % respectively.

In all of the measurements, the relative error related to the accuracy of attenuation and scatter correction is respectively smallest for images with both corrections applied. The relative error is 43 and 135 % smaller compared to images with only attenuation correction and images with no corrections applied respectively (SBR of 4:1, Table 4.10). For SBR of 8:1, the relative error is 27 and 114 % smaller in images with both corrections applied compared to images with only attenuation correction and images with no corrections applied respectively (Table 4.12).

4.2.4 Image quality results using different matrix sizes

In order to investigate how different image matrix sizes affect image quality, the first acquired data set with a SBR of 8:1 was reconstructed with both a matrix size (MS) of 168 x 168 pixels and a MS of 128 x 128 pixels. The remaining reconstruction parameters were kept as in the standard whole body PET/CT protocol. The image quality results from the two analyses are compared in table 4.13.

The differences in contrast recovery between the MS of 168 and 128 are between 1 % (37 mm cold contrast sphere) and 16 % (28 mm cold contrast sphere). There is no unambiguous pattern between the two matrix sizes. The contrast recovery coefficient is higher in an average of 8 % in some of the spheres (13, 22 and 37 mm sphere) for images reconstructed with a MS of 168 x 168 pixels. On the other hand, the 128 MS resulted in an average of 11 % higher contrast recovery for the 10, 17 and 28 mm spheres.

Besides the contrast recovery, table 4.13 also shows the background variability and the relative error connected to the lung insert for the two different matrix sizes. MS of 128 x 128 pixels results in 40 % higher background variability in the hot spheres (10 – 22 mm spheres) than the MS of 168 x 168 pixels. For the 37 mm cold sphere, the differences in background variability are 25 % smaller for the MS of 128 x 128 pixels and for the 28 mm cold sphere the background variability is equal (28 mm sphere) for both matrix sizes. The residual error from attenuation and scatter correction is 24 % larger with a MS of 168 x 168 pixels compared to MS of 128 x 128 pixels.

Table 4.13: NEMA Image quality results for 8:1 sphere-to-background ratio and Gaussian filters with FWHMs of 5 mm and matrix sizes of 168 x 168 and 128 x 128 pixels respectively. The 28 and 37 mm spheres are filled with non-radioactive water (cold contrast) while the remaining spheres are filled with a solution of F-18 (hot contrast).

Sphere diameters	Contrast recovery coefficient (%)		Background variability (%)	
	Matrix size 168	Matrix size 128	Matrix size 168	Matrix size 128
10 mm	7.9	8.8	4.6	6.5
13 mm	24.0	21.6	3.6	5.1
17 mm	37.1	39.0	3.4	5.0
22 mm	48.7	43.4	2.9	3.8
28 mm	50.8	58.7	3.0	3.0
37 mm	55.3	54.8	3.0	2.4
Lung insert relative error			28.0 %	22.6 %

4.3 Image quality results using an automatic Python routine

Table 4.14 below shows image quality results obtained by the Python program designed for the analysis of the NEMA IEC body phantom images as described in subtopic 3.5 in Chapter 3. The automatic analysis was conducted on images reconstructed with different Gaussian FWHMs from the first experiment with a SBR of 8:1. The corresponding image quality results from the manual analysis are given in table B.5 in Appendix B.

As for the manual analysis, table 4.14 shows that the contrast recovery coefficient increases with increasing sphere diameter for both hot and cold spheres (10 – 37 mm) in all analyses. The table also shows that the contrast recovery coefficient increases when the FWHM decreases (7 – 3 mm). On the average, the contrast recovery coefficient increases by 28 % for the hot spheres (10 – 22 mm) and 6 % for the cold spheres (28 and 37 mm) as the FWHM reduces from 7 to 3 mm. The background variability decreases with increasing sphere diameter (10 – 37 mm) and with increasing Gaussian FWHM. The residual error caused by attenuation and scatter correction show less difference between the FWHM of 3, 5 and 7 mm.

Figures 4.5(a) – 4.5(c) (Appendix C) compares the image quality results from the automatic analysis in table 4.14 with the manual analysis in table B.5 (Appendix B). In figure 4.5(a), the contrast recovery is averagely less than or equal to 26 % higher in some of the hot and cold spheres (10, 13, 17 and 28 mm) in images analyzed manually compared to images analyzed with the automatic python program for FWHMs of 3 mm. The contrast recovery is

however 3 % lower in the 22 and 37 mm spheres in images analyzed manually compared to images analyzed with the automatic python program for FWHMs of 3 mm.

In figure 4.5(b), the contrast recovery is averagely less than or equal to 21 % higher in some of the hot and cold spheres (10, 13, 17 and 28 mm) in images analyzed manually compared to images analyzed with the automatic python program for FWHMs of 5 mm. The contrast recovery is however 3 % lower in the 22 and 37 mm spheres in images analyzed manually compared to images analyzed with the automatic python program for FWHMs of 5 mm.

In figure 4.5(c), the contrast recovery is higher with an average less than or equal to 18 % in all the hot spheres as well as the 28 mm cold spheres in images analyzed manually than in images analyzed with the automatic python program for FWHMs of 7 mm. The contrast recovery is however 5 % lower in the 37 mm sphere in images analyzed manually compared to images analyzed with the automatic python program for FWHMs of 7 mm.

Table 4.14: NEMA Image quality results analyzed with a python program for 8:1 sphere-to-background ratio and Gaussian filters with FWHMs of 3, 5 and 7 mm respectively. The 28 and 37 mm spheres are filled with non-radioactive water (cold contrast) while the remaining spheres are filled with a solution of F-18 (hot contrast).

Sphere diameters	Contrast recovery coefficient (%)			Background variability (%)		
	FWHM 3 mm	FWHM 5 mm	FWHM 7 mm	FWHM 3 mm	FWHM 5 mm	FWHM 7 mm
10 mm	8.6	7.7	6.2	3.3	3.0	2.6
13 mm	20.8	18.9	15.4	3.0	2.8	2.5
17 mm	29.7	27.8	24.2	2.8	2.6	2.3
22 mm	45.6	43.5	39.4	2.6	2.5	2.2
28 mm	51.4	50.6	48.5	2.4	2.3	2.1
37 mm	57.7	56.7	54.9	2.1	2.0	2.0
Lung inserts (relative error)				32.9 %	33.1 %	33.5 %

The background variability is higher in all spheres (10 – 37 mm) and all FWHMs (3 – 7 mm) for images analyzed manually compared to the automatic python program. The manually analyzed background variability results were averagely 81, 64 and 54 % higher than the automatic python program analyzed results for FWHMs of 3, 5 and 7 mm respectively. The residual error from attenuation and scatter corrections are 46, 47 and 45 % respectively higher in the automatic python program analyzed results compared to the manual analysis for FWHMs of 3, 5 and 7 mm.

5. DISCUSSION

In this study, the image quality of PET images of a NEMA IEC Body Phantom was evaluated by investigating how combination of different reconstruction parameters affect the contrast recovery of spheres filled with radioactive F-18 solution embedded in a background with less activity concentration. Image noise was also evaluated by calculating background variability together with the accuracy of the image corrections applied (residual error) for the different experimental setups. According to [34], high image contrast is a feature of PET images and image quality is assessed by the image contrast. In this chapter, the image quality results obtained will be discussed as well as factors that might have influenced these results.

Image quality following the NEMA NU 2-2007 protocol

In accordance with the NEMA NU 2-2007 protocol, the IEC Body Phantom was prepared and scanned with the standard clinical whole body PET/CT protocol. The measured activity concentrations and filling processes are explained and presented in Chapter 3.1. Also, the parameters involved in the data acquisition and reconstruction process are listed in table 3.1, Chapter 3.2.

The average sphere-to-background activity concentration ratio (SBR) measured from the three experiments performed for each concentration ratios of 4:1 and 8:1 were respectively 5 % and 6 % higher than the recommended ratios. When preparing the phantom, the background activity was measured first, and the hot spheres activity was measured at a later time aiming at a sphere activity of 4 or 8 times the activity in the background. To reach an exact activity concentration ratio of 4:1 and 8:1 was challenging because of the uncertainties in both measuring, decay correcting and mixing the activity.

The image quality results obtained for SBR of 4:1 (Table 4.2, Chapter 4) showed that the hot contrast recovery coefficient increased with increasing sphere diameters, from 13.7 % for the 10 mm sphere to 42.6 % for the 22 mm sphere. The cold contrast sphere with diameter 37 mm also had slightly higher contrast recovery coefficient compared to the 28 mm cold contrast sphere. When visually inspecting the phantom images it is apparent that the larger the sphere, the easier detectable it is. Larger spheres will cover more image pixels/voxels than smaller spheres, and will therefore be easier detectable. But the effect causing smaller

spheres to have poorer contrast recovery than larger spheres is the so-called "partial-volume effect" (PVE). According to [35] and [36], PVE is caused by the limited resolution in PET images and the image sampling process. Since the distributions of radiotracers in PET are sampled on voxel grid, the voxel's contour mismatch with the actual tracers' distribution contours due to spill-out. The radioactive concentrations inside the hot spheres in this study therefore spill-out into the background concentration. There is also spill-in where radioactivity from outside (background) spill into the spheres, however this compensates only partially to the spilling out and makes the two processes unbalanced. Besides spilling out, PVE depends on sphere size. Signal intensities are underestimated especially in the smaller spheres and smaller spheres/tumours will therefore have a larger underestimation of activity concentration than larger spheres/tumours [35][36].

The results for 8:1 SBR (Table 4.4, Chapter 4.1.2) shows the exact similar trend concerning sphere diameter and contrast recovery. According to equations {3.1} and {3.2} (Chapter 3.4), the contrast recovery value is normalised for the SBR. The contrast recovery coefficient is therefore expected to be in the same value range for different SBRs. When comparing the mean recovery results for the 8:1 and 4:1 SBR (Table 4.2 and 4.4) the three smaller hot spheres (10 – 17 mm) seemed to have somewhat higher contrast recovery, but lower contrast recovery for the largest hot sphere (22 mm) and the two cold spheres. Taking into account the standard deviations in the contrast recovery measurements, these differences are probably less significant. The differences are more likely to be caused by uncertainties in mixing and measurements of F-18 together with statistical variations in measured counts.

Table 5.1: Comparison between analysis made in this project work with similar work done in this field.

Parameters	Project work	Bergmann et al
Scanner	Siemens Biograph	Siemens Biograph
Reconstruction Algorithm	Iterative reconstruction	Iterative reconstruction
Iterations	4	2
Subsets	8	8
Filter	Gaussian	Gaussian
FWHM (mm)	5	5
Background activity (kBq/cc)	5.237	5.5
Acquisition time (min)	3	7
Pixel size (mm)	5.326	3.38
Slices	108	47
Matrix size (pixels)	128 x 128	128 x 128
Concentration ratio		

SBR 4:1 Contrast recovery coefficients (Background Variability) Spheres: 10 mm	4.2 (%)	4.2 (%)
13 mm	15.2 (6.5)	14.0 (27.3)
17 mm	16.5 (5.8)	26.0 (20.6)
22 mm	26.2 (3.8)	37.0 (13.7)
28 mm	40.1 (3.5)	46.0 (11.6)
37 mm	57.7 (3.1)	57.0 (9.6)
	59.7 (2.4)	61.0 (9.6)

The background variability can be considered as an approximation of image noise. The background variability measured for both concentration ratios shows that the variability increases as the diameter of the sphere decrease. Fewer pixels will be encountered in the ROI of the smaller sphere, leading to higher statistical variations (higher standard deviation). The mean background variability for SBR of 4:1 and 8:1 are in the same value range (Tables 4.2 and 4.4). This gives the reason to assume that the background activity in the phantom approximates a homogeneous solution.

The residual error measured in the lung insert is associated with the accuracy of the attenuation and scatter corrections. The cylindrical lung insert was filled with only polystyrene beads and non-radioactive water as described in Chapter 3.1.1. In an ideal imaging representation, the measured mean counts in the lung insert should therefore approach zero. However, since the image correction for attenuation and scatter can never be exact, the measured mean counts in the lung insert appear to be higher than zero. Also, referring to the partial-volume effect explained above, spill-out from background and spheres into the lung insert might contribute to the residual error in the lung insert. Comparing Tables 4.2 and 4.4, the residual error was 9 % higher in the SBR of 8:1 than the SBR of 4:1. For a SBR of 8:1, there will be a higher total amount of activity in the phantom and consequently a higher number of positrons that can travel into the lung insert and annihilate from within the lung insert. The total number of photons will also increase with increasing activity which again will increase the amount of scattered photons. These effects will probably affect both attenuation and scatter correction.

The standard deviations of measured contrast recovery, background variability and lung insert relative error show fluctuations associated with repetitive experiments. From table 4.2

for SBR of 4:1, the standard deviation incorporated in the contrast recovery coefficient and background variability are less than or equal to 4.3 and 0.6 % respectively. From Table 4.4 for SBR of 8:1, the standard deviation in the contrast recovery coefficient and background variability, are respectively less than or equal to 6.8 % and 1.1 %. The standard deviations are related both to count statistics, variations in ROI positioning during image analysis and to accuracy of the activity measured and placed in the phantom in each experiment.

In table 5.1, the results obtained in this work following the NEMA standard are compared to measurements done by Bergmann et al. [34] on a similar scanner (Siemens Biograph). There are some variation in both acquisition parameters (time) and reconstruction parameters (number of iteration and subsets, pixel size), which makes a direct comparison of the contrast recovery results difficult. The analysis made by [34] was done using combination of automatic programming tools. They used ImageJ [34] programming tool to position the spheres in the image and the analysis was done using MATLAB and SPSS (Statistical Product and Service Solution) programming tools.

Bergmann et al. have measured somewhat higher recovery for most of the spheres and higher background variability for all of the spheres, compared to this work. But given the differences in acquisition settings, reconstruction parameters and analysis method, the recovery results seems overall to be in the same range on the two scanners.

Image quality when different Gaussian filter widths (FWHM) were used

The acquired data sets for both the 4:1 and 8:1 SBRs were all reconstructed with a Gaussian filter and different FWHMs (3, 5 and 7 mm) respectively. The other reconstruction parameter (iterative reconstruction with 4 iterations and 8 subsets, matrix size of 128 and zoom of 1) were kept constant. The measured contrast values increases as the FWHM decreases from 7 to 3 mm (Figures 4.1 to 4.4, Chapter 4.2.1) for both concentration ratios. The improvement in contrast recovery with decreasing FWHM was more prominent for the smaller hot spheres for both 4:1 and 8:1 SBR. The improvement was also more prominent for the 4:1 SBR compared to the 8:1 SBR.

A Gaussian filter with a smaller FWHM has a Gaussian fit curve with a smaller width. As the FWHM of the Gaussian filter increases, the smoothing strength of the filter is also

increased (more noise is removed) but it will also lead to increased image blurring. A decrease in FWHM results in less blurring of the image but less noise will also be removed. When the width of the Gaussian fit curve decreases, the filter is able to compute fewer voxels/regions in the image which is capable of producing less error than computing larger voxel regions. In that regard small tumour in clinical imaging may benefit if 3 mm FWHM is used instead of FWHMs of 5 and 7 mm, especially when the image contrast is poorer.

Image quality when different reconstruction filters were used

A selection of the image filters available on the Siemens Biograph scanner (Gaussian filter, Median filter, Hann filter and Butterworth filter) were used to reconstruct the acquired data set so that observations could be made on how each filter influence the image quality. All filters were used with a FWHM of 5 mm, so that they could be compared with the standard clinical protocol parameter.

All the filters used gave higher contrast values for bigger spheres and lower values for smaller spheres as explained using the Gaussian filter above. Meanwhile the Butterworth filter (order of 10) measured higher contrast values compared to the other filters for all hot contrast spheres (10 – 22 mm) and for both concentration ratios, followed by Gaussian filter, Hann filter and lastly median filter (Tables 4.8 – 4.8, Chapter 4.2). The Butterworth (O10) and Hann filters have both cut-off frequencies which aid in speeding the filtering process by removing high frequencies which may cause more noise in the image. In addition, the Butterworth filter also has a user defined order which adjusts the strength of the filter in the sense that the higher the order (O), the more rapidly the filtering is done to produce a result.

There were less differences and no recognizable pattern in the measured contrast values for the cold contrast spheres (28 and 37 mm) with varying image filter type.

The background variability measured somewhat higher values for the Butterworth filter (O10) compared to the other filters. This may lead to the conclusion that although the Butterworth filter results in higher image contrast recovery it also results in higher image noise/ background variability. The Gaussian filter which had the overall second highest contrast recovery values, had less background variability compared to the Butterworth filter.

Selection of image filter seems therefore to be a trade-off between image contrast recovery and background noise.

Image quality when different image corrections were used

To compare image quality in relation to different image corrections, image quality analysis were done on images with both attenuation and scatter correction applied, only attenuation correction applied and no correction applied. The purpose of attenuation correction as described in Chapter 2.9.1 is to correct for the attenuation of photons throughout the object and the purpose of scatter correction (Chapter 2.9.2) is to correct for the photons that are scattered after the positron annihilation process, but yet detected as a true coincident. For SBR of 4.1 in table 4.10, images corrected with both attenuation and scatter resulted in hot contrast recovery coefficients that were averagely 11 and 366 % greater than the same image data set corrected with only attenuation correction and no corrections respectively. The cold contrast recovery was highest for the uncorrected images followed by the images with both corrections and the only attenuation corrected images, respectively.

Similar results are found for SBR of 8:1 as given in table 4.12. Images corrected with both attenuation and scatter had respectively 22 and 85 % higher hot contrast values than images with only attenuation correction and no correction. The cold contrast recovery is 116 % higher in images with both corrections applied than in only attenuation corrected images. Yet, the cold contrast recovery is 40 % lower in images with both corrections applied than in uncorrected images.

The contrast recovery is higher in images corrected with both corrections for both SBRs because the photons attenuated and scattered (Chapters 2.9.1 and 2.9.2) are somewhat removed from the images. This also shows why only attenuation corrected images higher contrast recoveries than non-corrected images have since the scattered photons are in this case removed from the images. There is no activity in the cold spheres which suggests that there would also be no attenuated or scattered photons, and this reason might have influenced the contrast recovery measured in both the attenuation and scatter corrected images and only attenuation corrected images.

The background variability computed for the hot spheres in table 4.10 are in average of 390 and 234 % higher in non corrected images than both attenuation and scatter and only attenuation corrected images respectively. The difference gets larger (829 and 432 %) in the 28 and 37 mm spheres in non corrected images than both attenuation and scatter and only attenuation corrected images. As discussed above for the contrast recovery, in the non-corrected images, the attenuated and scattered photons contribute to the noise in the image and thus increase the background variability. So far as these attenuated and scattered photons are not removed in the image correction processes described in Chapters 2.9.1 and 2.9.2, the background variability measured higher values in non-corrected images.

Image quality when different matrix sizes were used

In table 3.2, the standard matrix size (MS) used in the clinical protocol is 168 x 168 pixels. Due to error on my side during image acquisition, a MS of 128 x 128 pixels was used throughout the experiments. Nevertheless, the 168 x 168 pixels MS was employed and compared to the MS of 128 x 128 pixels, keeping the other parameters in table 3.2 constant. The results presented in table 4.13 (Chapter 2.4.2) does not show any defined pattern between the two matrix sizes. The 168 MS has an average of 8 % higher contrast recovery coefficient in the 13, 22 and 37 mm spheres compared to that of the 128 MS. According to the theory presented in Chapter 2.8.4 a matrix size of 128 x 128 pixels will have bigger pixels than a matrix size of 168 x 168 pixels. The bigger the MS (smaller pixels), the more detailed the image becomes thereby increasing spatial resolution. There is no clear trend from the obtained contrast recovery results and the two MS (and thereby spatial resolution).

The result in table 4.13 shows that the background variability is averagely 40 % higher (10 – 22 mm spheres) and 25 % lower (37 mm sphere) in the 128 MS compared to the 168 MS. It was however expected that MS of 128 x 128 pixels should have greater background variability than the 168 MS. The reason for this claim is that an image with less MS will have greater statistical error which will increase the background variability than a bigger MS.

Image quality when an automatic Python routine was used

One aspect of this work is to analyse some of the data sets with an automatic Python program designed for the analysis of the NEMA IEC body phantom images (Chapter 3.5).

The Python program developed by [31], was in this work used to analyse images reconstructed with Gaussian filter with FWHMs of 3, 5 and 7 mm. Overall the image quality results obtained with the automatic analysis program (table 4.14, Chapter 4.3) was consistent the image quality results obtained in the manual analysis. This confirms the assumption made earlier that a Gaussian filter with smaller FWHM will have higher contrast recovery than when the FWHM is bigger.

Also as expected, the smaller sphere will have higher background variability which is due to bigger statistical error in computing few counts in the spheres. For all three FWHMs (3, 5 and 7 mm), the background variability was highest in the smaller spheres and decreases as the sphere diameter decrease. However, from the FWHM of 7 to 3 mm, the background variability increased by 17.6 %.

From figures 4.5(a) – 4.5(c), it can be noticed that the contrast recovery coefficient is higher in the three smaller hot spheres and lower in the 22 mm hot sphere and the two cold spheres for images analyzed with the automatic python program compared to the manual analyses. The recovery is averagely 22 % higher in the three smaller spheres and 4 % lower in the three bigger spheres for images analyzed with the automatic python program compared to the manual analyses. The differences in the contrast recovery values measured between the automatic python program and the manual analyzes may be as a result of the number of pixels in a particular ROI. According to the NEMA protocol, section 7.4.1 and [31], the python program includes more pixels/ partial pixels that lie within a ROI. The manner in which the Siemens work station includes pixels/ parts of pixels is unknown. The partial pixels includes in the automatic program ROI's peripheral might have caused the lower contrast recovery values measured. Since the contrast recovery is higher in usually the smaller spheres for manually analyzed images, it might be that this number of pixels in a ROI's peripheral effect is more prominent in smaller spheres.

Unlike the manual analyses which are time consuming and influenced by ROI sizing and placing, the analyses made by the use of the automatic python program is quick (less than a minute processing time on one data set) and gives reproducible results.

CONCLUSION

In this work, a NEMA IEC body phantom was used which consist of a body phantom, lung insert, six spheres of various sizes connected to a lid that fits into the body phantom and a scanner extension phantom. Analyzes has been made on data sets obtained from different reconstruction parameters employed in the image reconstruction process. The comparison of analyzes made with different reconstruction parameters demonstrates the assessment of measuring the image quality of PET/CT system by determining the image contrast. The results obtained from the study shows substantially variations in image quality when different reconstructions are employed other than the daily clinical protocol.

In general the study shows the contrast recovery coefficient increases with increasing sphere size. This contrast values in the various sphere sizes were expected due to the effect of PVE. The contrast recovery also increases as the FWHM (using a Gaussian filter) decreases. On the other hand, it was expected that the contrast recovery should be in the same range for different SBRs. However, there is no regular pattern in the measured contrast values. These differences are more likely to be caused by uncertainties in mixing and measurements of F-18 together with statistical variations in measured counts.

The background variability values measured showed that as the size of the sphere increases, the background variability decreases. These measured values confirm the effect of PVE.

The study allows for suggestions to improve concerning performance of the PET/CT system and also the capability of exchanging PET reconstruction parameters. The use of the automatic python program was to determine the accuracy of the manual analysis and also to determine the reproducibility of the designed program.

REFERENCES

[1] Vallabhajosula, Shankar (2009) Molecular Imaging: Radiopharmaceuticals for PET and SPECT. PET and SPECT scanners: Introduction of radiation with matter. New York, Springer, pp.59 - 81, May.

[2] Richard, L. W. and Others (2008) *Technical Considerations for PET/CT and SPECT/CT: The PET Component of the PET/CT Scanner*. In: Richard, L. W. and Ora, I. ed. *Atlas of PET/CT with SPECT/CT*. Philadelphia, Saunders, pp.2 - 11.

[3] Timothy G. Turkington (2009) *PET Physics and PET Instrumentation.* In: Lippincott Williams and Wilkins; Richard, L. W. ed., Robert S. B. Beanlands ed. *Principles and Practice of PET and PET/CT*. 2nd Ed. Philadelphia, Lippincott Williams and Wilkins, p.48, 70.

[4] K. Wechalekar, B. Sharma, G. Cook (2005) *PET/CT in Oncology – A major advance. Clinical Radiology (2005)*, 60. pp.1143 - 1155.

[5] NEMA NU 2-2007 (2007), Performance Measurement of Positron Emission Tomography. National Electrical Manufacturers Association (NEMA).

[6] Kim Greer, C. N. M. T. (2002 – 2008) NEMA IEC body Phantom set user's manual. Data Spectrum Cooperation.

[7] Christiane B. and Ute F., Siemens Biograph PET/CT scanner: SOMATOM Sensation 40/64 Application guide.

[8] Siemens Biograph PET/CT scanner at the PET centre at the Hukeland University Hospital, Bergen – Norway.

[9] Perry Sprawls Jr. (1995) *Physical Principles of Medical Imaging. Interaction of Radiation with Mather*, 2nd Ed. p.149-150

[10] Chris, S. and Toby, B. (2001) *Fundamentals of Digital Imaging Processing*. pp.

[11] Russ, J. C. (1998) *The Image Processing Handbook*: 3rd Ed. CRC Press, CRC Press LLC.

[12] Gonzalez, R. C. and Woods, R. E. (2008) *Digital Image Processing*. 2nd ed. NY, Prentice Hall, Upper Saddle River.

[13] Leo, W. R (1992) *Techniques for Nuclear and Particle Physics Experiments: Statistics and the Treatment of Experimental Data*. Springer Verlag Berlin Heidelberg.

[14] Davies, E. (1990) *Machine Vision: Theory, Algorithms and Practicalities*, Academic Press, pp. 42 – 44

[15] Gengsheng, L. Z. (2010) *Medical Image Reconstruction*. Beijing and Springer-Verlag, Berlin Heidelberg, Higher Education Press.

[16] Smith, S. W. (1997 - 1999) *The Scientist and Engineer's Guide to Digital Signal processing*. 2nd Ed. California Technical Publishing.

[17] Sharp, P. F. and Goatman, K. A. (2005). Practical Nuclear Medicine. Nuclear Medicine Imaging. P. F. Sharp, H. G. Gemmell and A. D. Murray. 3rd ed. Singapore, Springer–Verlag London Limited.

[18] Cherry, S. R., Sorenson, J. A. and Phelps, M. E. (2012) Physics in Nuclear Medicine. 4th Ed. Philadelphia, Saunders.

[19] Bushberg, J. T., Seibert, J. A., Leidholdt, E. M. And Boone J. M. (2002) Computed Tomography. The Essential Physics of Medical Imaging, 2nd Ed. Philadelphia, Lippincott Williams and Wilkins, pp. 327 – 329.

[20] Cooke, C. D. et al (2011) Fundamentals of Image Processing in Nuclear Medicine: Image Filtering. In: Khalil, M. M. ed. *Basic Science of Nuclear Medicine*. Springer Verlag Berlin Heidelberg

[21] Tae Hyun Yoon et al (2009) Butterworth Window for Power Spectral Density Estimation. *ETRI Journal*, 31 (3) June, p. 293.

[22a] Saha, G. B. (2005) *Basics of PET Imaging: Image Reconstruction, Storage and Display*. New York, Springer Science and Business Media, Inc.

[22b] Saha, G. B. (2005) *Basics of PET Imaging: Radioactive Decay and Interaction of Radiation with Matter*. New York, Springer Science and Business Media, Inc.

[22c] Saha, G. B. (2005) *Basics of PET Imaging:* Cyclotron and Production of PET Radionuclides. New York, Springer Science and Business Media, Inc.

[22d] Saha, G. B. (2005) *Basics of PET Imaging:* Synthesis of PET Radiopharmaceuticals. New York, Springer Science and Business Media, Inc.

[23] Dominik Fehlker (2009) PET project. [wikihost.uib.no/ift]

[24a] Caramelo, F. J., Guerreiro, C., Ferreira, C. N., and Crespo, P. (2011) Radiation Detectors and Image Formation. In: Pedroso de Lima, J. J. ed. *Nuclear Medicine Physics.* New York (U. S), CRC Press, pp. 133 – 202.

[24b] Fracisco, J. C. Alves (2011) Cyclotron and Radionuclide Production. In: Pedroso de Lima, J. J. ed. *Nuclear Medicine Physics.* New York (U. S), CRC Press, pp. 10 – 33.

[25] Robert, F. et al (2004) [Accessed: February, 2013 from http://homepages.inf.ed.ac.uk/rbf/HIPR2/hipr_top.htm]

[26] Leow Wee Kheng, Image Processing: CS4243 Computer Vision and Pattern Recognition. National University of Singapore.

[27] PodgorŠak, E.B.(2010) Biological and Medical Physics, Biomedical Engineering. 2nd Edition, Springer-Verlag Berlin Heidelberg.

[28] Jostein Sæterstøl (2010) Characterization of Scintillation Crystals for Positron Emission Tomography.

[29] Sorenson, J. A. and Phelps, M. E. (1987) Physics in Nuclear Medicine. 2nd Ed. Elsevier Inc. - Health Sciences Division.

[30] Scientific sentences (2010) Attenuation Coefficients [Accessed: July, 2013 from http://scientificsentence.net/Radiations]

[31] Njål, Brekke (2013) Automatic python program for analysing NEMA IEC body phantom images. Haukeland University Hospital at Bergen, Norway.

[32] Lois Romans (2013) CT Image Quality [Accessed: July, 2013 from http://www.cewebsource.com/coursePDFs/CTimageQuality.pdf]

[33] Lee W. Goldman (2007) Principles of CT: Radiation Dose and Image Quality. Journal of Nuclear Medicine Technology, Vol. 35, no. 4; pgs.213 – 225.

[34] Bergmann et al. (2005) An inter-laboratory comparison study of image quality of PET scanners using the NEMA NU 2-2001 procedure for assessment of image quality. Institute of Physics Publishing, Physics in medicine and Biology, pgs. 2193–2207.

[36] Turku PET Centre, Image processing: Partial-Volume Effect. [Accessed: July, 2013 from www.pet.fi]

[35] Stephen L. Bacharach and Irene Buvat (2007) Partial-Volume Effect in PET Tumor Imaging Marine Soret1. The journal of nuclear medicine .Vol. 48, No. 6; Pgs 932–945.

[37] Michael M. Graham (2011) Quantitation of PET Data in Clinical Practice. Nancy M. Swanston and Paul Shreve (2011) Patient Preparation and Management In Paul Shreve ed.and David W. Townsend ed. Clinical PET/CT in Radiology. Springer New York Dordrecht Heidelberg London.

[38] Biological True Point PET/CT Operation Guide. Daily Startup, pgs. 71 – 96.

.

APPENDIX A

Specification for NEMA IEC Body Phantom Set™ Model PET/IEC-BODY/P	
Model Number:	ECT/IEC-BODY/P
Interior length of phantom:	194 mm
Fillable spheres (6) inner diameters:	10 mm, 13 mm, 17 mm, 22 mm, 28 mm, and 37 mm
Distance from sphere plane to bottom plate:	70 mm
Volume of empty cylinder:	~ 9.7 litres
Sphere wall thickness:	1 mm
Cylindrical (lung) insert dimensions	
External diameter:	51 mm
Internal diameter:	44.5 mm
External length:	203 mm
Volume:	194 ± 1 ml
Density:	0.30 ± 0.10 g/cc
Diameter of sphere opening:	1.5 mm
Test phantom dimension	
Length of cylindrical test phantom:	
Length of line source:	700 ± 5 mm
Volume of line source:	5.6 millilitres (ml)

Volume of NEMA IEC Body Phantom Set™ Compartments Model ECT/IEC-BODY/P		
Compartment	Ideal (Manufactured) Volume	My Measured Volume
10 mm Sphere	0.5 ml	0.58 ml
13 mm Sphere	1.15 ml	1.20 ml
17 mm Sphere	2.57 ml	2.60 ml
22 mm Sphere	5.57 ml	5.50 ml
28 mm Sphere	11.49 ml	11.40 ml
37 mm Sphere	26.52 ml	27.00 ml
Lung Insert	194 ml	110 ml
Torso Cavity	9.7 litres	9.708 litres

APPENDIX B

Table B.1: NEMA Image quality results for the third experiment with 4:1 sphere-to-background ratio and Gaussian filters with FWHMs of 3, 5 and 7 mm respectively. The 28 and 37 mm spheres are filled with non-radioactive water (cold contrast) while the remaining spheres are filled with a solution of F-18 (hot contrast).

Sphere diameters	Contrast recovery coefficient (%)			Background variability (%)		
	FWHM 3 mm	FWHM 5 mm	FWHM 7 mm	FWHM 3 mm	FWHM 5 mm	FWHM 7 mm
10 mm	17.5	14.2	11.3	8.6	6.5	4.9
13 mm	20.5	16.5	13.0	7.6	5.8	4.4
17 mm	28.0	26.2	23.1	4.8	3.8	3.3
22 mm	42.1	40.1	37.3	4.3	3.5	3.0
28 mm	58.9	57.7	55.6	4.0	3.1	2.7
37 mm	59.4	59.3	55.6	3.0	2.4	2.3
Lung inserts (relative error)				21.8 %	21.9 %	22.8 %

Table B.2: Mean values and standard deviation of three repetitive NEMA Image quality experiments for 4:1 sphere-to-background ratio and Gaussian filters with FWHMs of 3, 5 and 7 mm respectively. The 28 and 37 mm spheres are filled with non-radioactive water (cold contrast) while the remaining spheres are filled with a solution of F-18 (hot contrast).

Sphere diameters	Mean Contrast recovery coefficient (%)			Background variability (%)		
	FWHM 3 mm	FWHM 5 mm	FWHM 7 mm	FWHM 3 mm	FWHM 5 mm	FWHM 7 mm
10 mm	15.2 ± 2.8	13.7 ± 1.8	8.9 ± 1.6	8.9 ± 0.1	6.8 ± 0.6	5.2 ± 0.1
13 mm	22.4 ± 3.2	20.2 ± 3.2	15.3 ± 1.3	7.3 ± 0.1	5.9 ± 0.4	4.4 ± 0.1
17 mm	32.7 ± 2.9	30.7 ± 4.3	26.8 ± 1.4	4.7 ± 0.3	4.0 ± 0.2	3.3 ± 0.0
22 mm	44.9 ± 2.8	42.6 ± 2.8	38.3 ± 1.2	4.5 ± 0.6	3.6 ± 0.3	3.1 ± 0.0
28 mm	58.8 ± 1.7	57.8 ± 1.3	54.7 ± 0.8	4.2 ± 0.2	3.1 ± 0.3	2.9 ± 0.1
37 mm	60.3 ± 1.4	60.1 ± 0.6	57.2 ± 1.9	3.0 ± 0.7	2.6 ± 0.5	2.1 ± 0.6
Lung inserts (relative error)				(21.8 ± 2.0) %	(22.0 ± 0.1) %	(22.7 ±1.4) %

Table B.3: NEMA Image quality results for the third experiment with 8:1 sphere-to-background ratio and Gaussian filters with FWHMs of 3, 5 and 7 mm respectively. The 28 and 37 mm spheres are filled with non-radioactive water (cold contrast) while the remaining spheres are filled with a solution of F-18 (hot contrast).

Sphere diameters	Contrast recovery coefficient (%)			Background variability (%)		
	FWHM 3 mm	FWHM 5 mm	FWHM 7 mm	FWHM 3 mm	FWHM 5 mm	FWHM 7 mm
10 mm	20.6	17.9	13.4	8.7	6.7	5.2
13 mm	24.0	21.9	18.5	7.1	5.9	4.7
17 mm	36.9	34.2	30.3	6.6	5.5	4.5
22 mm	41.7	39.7	36.6	5.4	4.5	3.8
28 mm	49.0	46.9	43.4	4.5	3.8	3.2
37 mm	54.5	52.6	49.4	3.4	3.0	3.3
Lung inserts (relative error)				21.7 %	24.9 %	25.5 %

Table B.4: Table B.2: Mean values and standard deviation of three repetitive NEMA Image quality experiments for 8:1 sphere-to-background ratio and Gaussian filters with FWHMs of 3, 5 and 7 mm respectively. The 28 and 37 mm spheres are filled with non-radioactive water (cold contrast) while the remaining spheres are filled with a solution of F-18 (hot contrast).

Sphere diameters	Mean Contrast recovery coefficient (%)			Background variability (%)		
	FWHM 3 mm	FWHM 5 mm	FWHM 7 mm	FWHM 3 mm	FWHM 5 mm	FWHM 7 mm
10 mm	18.4 ± 1.8	16.3 ± 6.8	13.0 ± 3.7	8.1 ± 0.2	6.5 ± 0.3	5.0 ± 0.1
13 mm	25.3 ± 2.3	22.8 ± 2.5	18.9 ± 2.5	6.5 ± 0.3	5.3 ± 0.5	4.3 ± 0.3
17 mm	37.3 ± 1.6	34.7 ± 3.2	31.0 ± 2.3	5.6 ± 0.8	4.6 ± 1.1	3.8 ± 0.1
22 mm	43.4 ± 1.7	41.9 ± 3.6	38.8 ± 2.3	4.8 ± 0.6	3.9 ± 0.3	3.3 ± 1.1
28 mm	52.7 ± 2.4	51.6 ± 2.7	48.4 ± 1.2	4.0 ± 0.6	3.4 ± 0.3	2.9 ± 0.5
37 mm	56.2 ± 2.3	55.0 ± 2.5	52.4 ± 1.7	3.2 ± 0.3	2.7 ± 0.2	2.7 ± 0.3
Lung inserts (relative error) %				(22.9 ± 0.5) %	(24.0 ± 0.2) %	(24.6 ± 0.3)

Table B.5: NEMA Image quality results analyzed manually for the first experiment with 8:1 sphere-to-background ratio and Gaussian filters with FWHMs of 3, 5 and 7 mm respectively. The 28 and 37 mm spheres are filled with non-radioactive water (cold contrast) while the remaining spheres are filled with a solution of F-18 (hot contrast).

Sphere diameters	Contrast recovery coefficient (%)			Background variability (%)		
	FWHM 3 mm	FWHM 5 mm	FWHM 7 mm	FWHM 3 mm	FWHM 5 mm	FWHM 7 mm
10 mm	10.5	8.8	6.8	8.0	6.5	5.2
13 mm	23.6	21.6	18.7	6.3	5.1	4.2
17 mm	41.8	39.0	34.8	6.0	5.0	4.1
22 mm	44.8	43.3	40.5	4.5	3.8	3.2
28 mm	59.8	58.7	55.2	3.6	3.0	2.6
37 mm	55.6	54.8	52.5	2.9	2.4	2.2
Lung inserts (relative error)				22.6 %	22.6 %	23.1 %

APPENDIX C

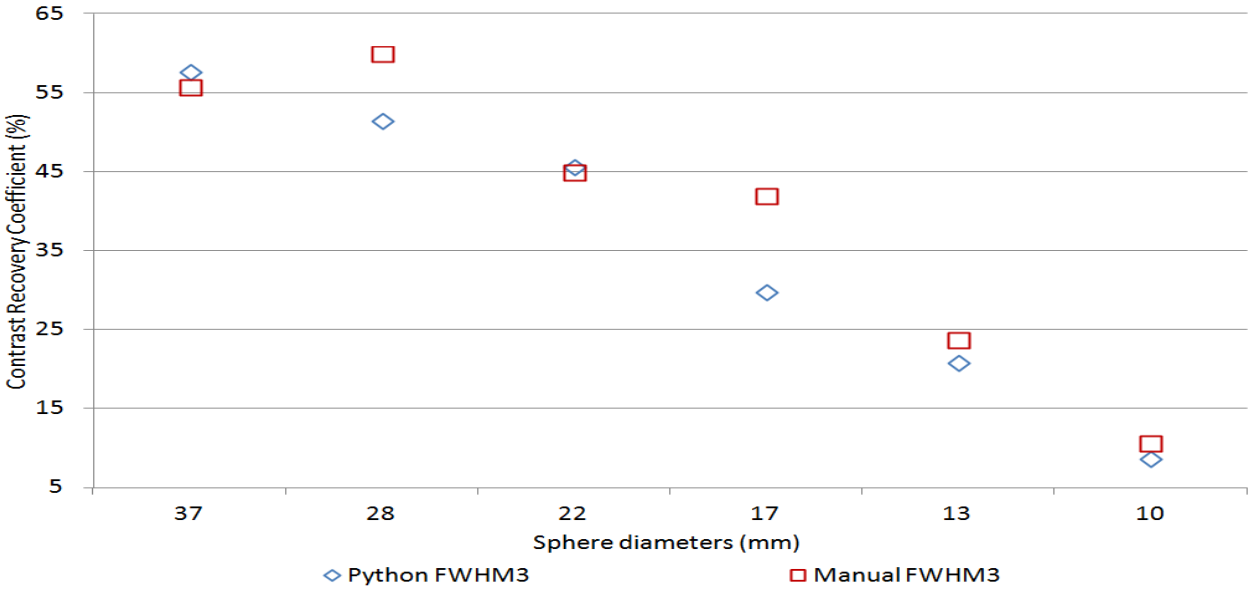

Figure 4.5(a): Comparison of contrast recovery coefficient values in images of the NEMA phantom analyzed both manually and the python program with a sphere-to-background ratio of 8:1. The images are reconstructed using Gaussian filters with FWHM of 3 mm. The 28 and 37 mm spheres are filled with non-radioactive water (cold contrast) while the remaining spheres are filled with a solution of F18 (hot contrast).

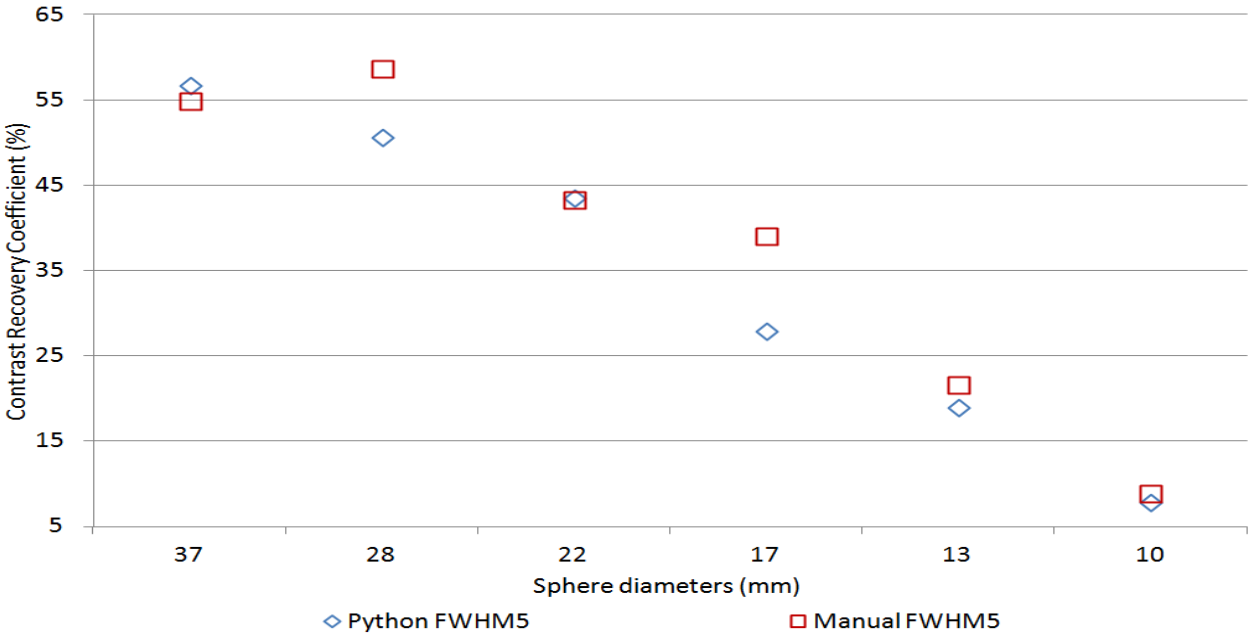

Figure 4.5(b): Comparison of contrast recovery coefficient values in images of the NEMA phantom analyzed both manually and the python program with a sphere-to-background ratio of 8:1. The images are reconstructed using Gaussian filters with FWHM of 5 mm. The 28 and 37 mm spheres are filled with non-radioactive water (cold contrast) while the remaining spheres are filled with a solution of F18 (hot contrast).

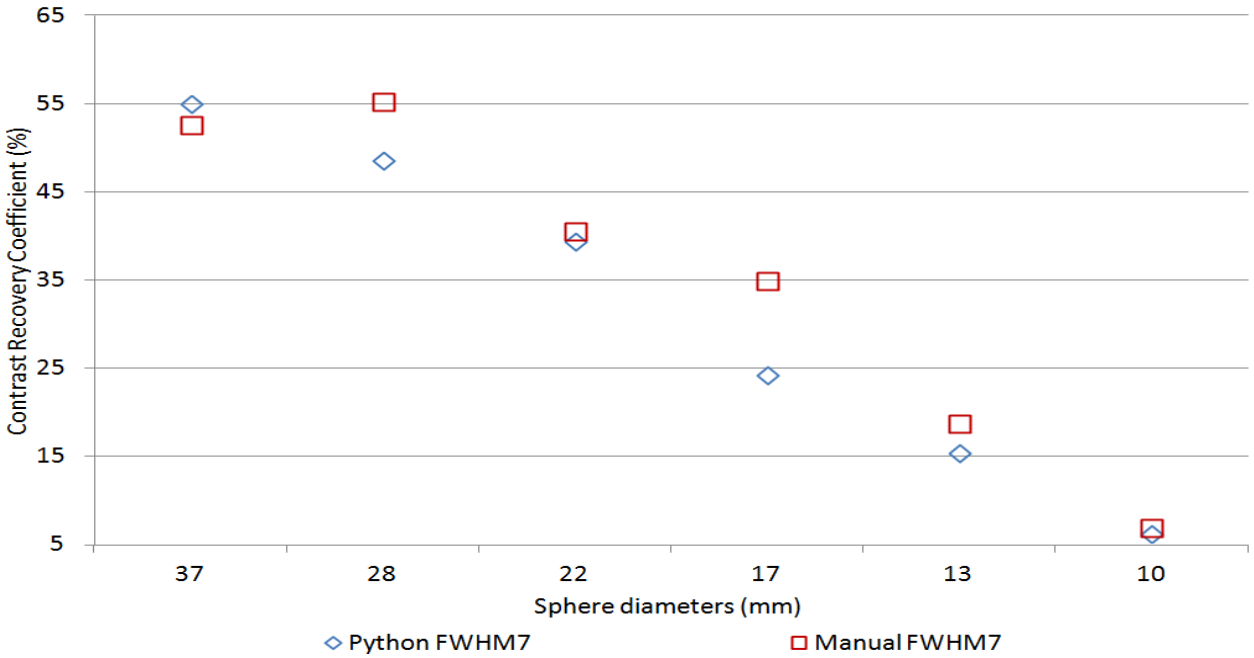

Figure 4.5(c): Comparison of contrast recovery coefficient values in images of the NEMA phantom analyzed both manually and the python program with a sphere-to-background ratio of 8:1. The images are reconstructed using Gaussian filters with FWHM of 7 mm. The 28 and 37 mm spheres are filled with non-radioactive water (cold contrast) while the remaining spheres are filled with a solution of F18 (hot contrast).